lipids and determination of phospholipids by phosphorus analysis of spots. Lipids *5*, 494–496.

12. Aoyama, C., Ohtani, A., and Ishidate, K. (2002). Expression and characterization of the active molecular forms of choline/ethanolamine kinase-α and -β in mouse tissues, including carbon tetrachloride-induced liver. Biochem. J. *363*, 777–784.
13. Wu, G., Aoyama, C., Young, S.G., and Vance, D.E. (2008). Early embryonic lethality caused by disruption of the gene for choline kinase alpha, the first enzyme in phosphatidylcholine biosynthesis. J. Biol. Chem. *283*, 1456–1462.
14. Wu, G., Sher, R.B., Cox, G.A., and Vance, D.E. (2010). Differential expression of choline kinase isoforms in skeletal muscle explains the phenotypic variability in the rostrocaudal muscular dystrophy mouse. Biochim. Biophys. Acta *1801*, 446–454.
15. Nakanishi, H., Iida, Y., Shimizu, T., and Taguchi, R. (2010). Separation and quantification of sn-1 and sn-2 fatty acid positional isomers in phosphatidylcholine by RPLC-ESIMS/MS. J. Biochem. *147*, 245–256.
16. Ikeda, K., Mutoh, M., Teraoka, N., Nakanishi, H., Wakabayashi, K., and Taguchi, R. (2011). Increase of oxidant-related triglycerides and phosphatidylcholines in serum and small intestinal mucosa during development of intestinal polyp formation in Min mice. Cancer Sci. *102*, 79–87.
17. Taguchi, R., Houjou, T., Nakanishi, H., Yamazaki, T., Ishida, M., Imagawa, M., and Shimizu, T. (2005). Focused lipidomics by tandem mass spectrometry. J. Chromatogr. B Analyt. Technol. Biomed. Life Sci. *823*, 26–36.
18. Wu, G., Sher, R.B., Cox, G.A., and Vance, D.E. (2009). Understanding the muscular dystrophy caused by deletion of choline kinase beta in mice. Biochim. Biophys. Acta *1791*, 347–356.
19. Miyagawa, T., Kawashima, M., Nishida, N., Ohashi, J., Kimura, R., Fujimoto, A., Shimada, M., Morishita, S., Shigeta, T., Lin, L., et al. (2008). Variant between CPT1B and CHKB associated with susceptibility to narcolepsy. Nat. Genet. *40*, 1324–1328.
20. Zweigner, J., Jackowski, S., Smith, S.H., Van Der Merwe, M., Weber, J.R., and Tuomanen, E.I. (2004). Bacterial inhibition of phosphatidylcholine synthesis triggers apoptosis in the brain. J. Exp. Med. *200*, 99–106.

Pediatric Neurology 45 (2011) 114–116

Contents lists available at ScienceDirect

Pediatric Neurology

journal homepage: www.elsevier.com/locate/pnu

Case Report

Anti-Signal Recognition Particle Myopathy in the First Decade of Life

Shigeaki Suzuki MD [a,*], Masayasu Ohta MD [b], Yuko Shimizu MD [c], Yukiko K. Hayashi MD [d], Ichizo Nishino MD [d]

[a] *Department of Neurology, Keio University School of Medicine, Tokyo, Japan*
[b] *Department of Pediatrics, Toride Kyodo General Hospital, Ibaragi, Japan*
[c] *Department of Pediatric Neurology, National Center Hospital of Neurology and Psychiatry, Tokyo, Japan*
[d] *Department of Neuromuscular Research, National Institute of Neuroscience, National Center of Neurology and Psychiatry, Tokyo, Japan*

ARTICLE INFORMATION

Article history:
Received 11 November 2010
Accepted 11 April 2011

ABSTRACT

Autoantibodies to signal recognition particle have been associated with juvenile and adult-onset necrotizing myopathy. However, only a few teenage patients with anti-signal recognition particle myopathy have been reported, and to date, to our knowledge, no patient younger than 10 years has been documented. We describe 2 Japanese girls with anti-signal recognition particle myopathy who developed symptoms from the ages of 5 and 9 years, respectively. Both patients had progressive muscle weakness and atrophy without myalgia. Facioscapulohumeral muscular dystrophy was initially suspected because of asymmetric shoulder girdle muscle involvement in one patient, and limb girdle muscular dystrophy due to proximal limb muscle weakness in the other. There were no extramuscular manifestations, including fever or arthritis. Serum creatine kinase levels were elevated to 2,467-4,629 IU/L. Results of muscle biopsy revealed necrotizing myopathy with minimal to mild endomysial fibrosis but without inflammatory infiltrates. Immunosuppressive agents were not effective for muscle weakness, resulting in marked disability. Anti-signal recognition particle myopathy can occur in the first decade of life and should be included in the differential diagnosis for children with progressive limb girdle muscle weakness and high creatine kinase levels.

Introduction

Among childhood idiopathic inflammatory myopathies, juvenile dermatomyositis is the most common, representing up to 85% of them [1], followed by polymyositis, which has a much lower incidence in childhood than in adulthood. To date, several myositis-associated autoantibodies have been associated with up to 40% of cases of juvenile idiopathic inflammatory myopathies [2,3].

Autoantibodies to signal recognition particle (SRP), one of the myositis-associated autoantibodies, were first found in the serum of an adult patient with polymyositis by the RNA immunoprecipitation method [4,5]. Previous studies revealed that positivity for anti-SRP antibodies occurred in 4-8% of adult patients and about 2% of children with inflammatory myopathies [6-11]. Clinically and histologically, anti-SRP antibody has been characterized by rapid progression of weakness, often culminating in severe disability, markedly raised serum creatine kinase (CK) levels, necrotizing myopathy without inflammation, and poor response to corticosteroid therapy [6-12]. However, these observations were mainly gathered from previous reports about adult patients.

Herein, we report 2 patients with anti-SRP myopathy whose ages at disease onset were in the first decade of life, and who both displayed phenotypes distinct from those of adult and juvenile patients.

Case Report

Patient 1

A 6-year-old Japanese girl was admitted to our hospital for evaluation of elevated serum CK level. She was apparently healthy until the age of 5 years, when her parents first noticed that she was falling frequently and becoming easily tired. She was also noted to be a slow runner in school. There were no anteceding signs of infection, including fever, malaise, or changes in appetite. Neurologic examination revealed proximal limb weakness and atrophy. She exhibited Gowers sign and waddling gait, especially when climbing stairs. Deep tendon reflexes and muscle tone were normal. Serum CK level was 2,410 IU/L (normal range 45-163 IU/L). A multiplex ligation-dependent probe amplification analysis for the dystrophin gene was normal, although genetic analysis for limb-girdle muscular dystrophy was not performed. Electromyography revealed myopathic features in the biceps brachii, quadriceps femoris, and tibialis anterior muscles. Over the course of 1 year, her muscle weakness progressed, and she eventually could not lift her thighs or get up

* Communications should be addressed to: Dr. S. Suzuki; Department of Neurology, Keio University School of Medicine, 35 Shinanomachi, Shinjuku-ku, Tokyo 160-8582, Japan.
E-mail address: sgsuzuki@z3.keio.jp

0887-8994/$ - see front matter © 2011 Elsevier Inc. All rights reserved.
doi:10.1016/j.pediatrneurol.2011.04.009

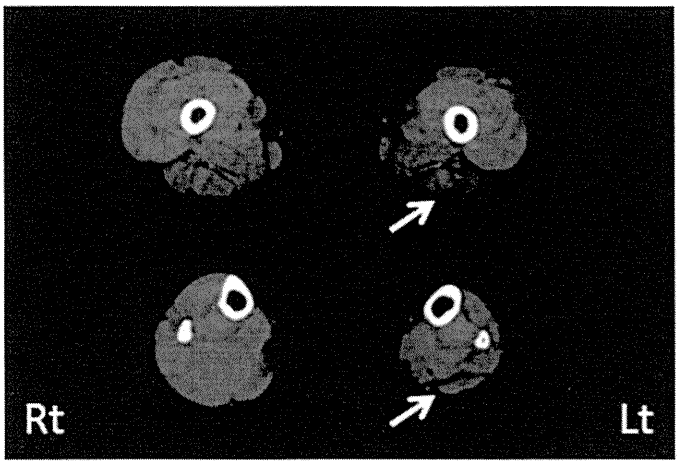

Figure 1. Muscle computed tomography of patient 2 at age 10 years revealing left-side dominant atrophy, especially in hamstring and gastrocnemius muscles (arrows).

from a supine position. The muscle atrophy in her arms, shoulders, and legs became more prominent. Serum CK was increased to 4,629 IU/L. Oral administration of prednisone (1 mg/kg per day) was initiated, and the serum CK level decreased to 640 IU/L. However, no improvement in the muscle weakness was observed.

Patient 2

A 10-year-old Japanese girl was admitted to our hospital for limb muscle weakness. She was well until the age of 9 years (7 months before admission), when she began to experience difficulty in raising her arms and running. She also fell down frequently. Neurologic examination revealed left-side dominant muscle weakness of the neck, shoulder girdle, and upper arms. She also had scapular winging. She exhibited a wide-based gait and could not walk more than 100 m, although Gowers sign was not evident. The deep tendon reflexes were normal. Serum CK level was elevated to 2,467 IU/L. Electromyography revealed myopathic changes in the biceps brachii, deltoid, and tibialis anterior muscles. Muscle computed tomography revealed left-side dominant atrophy especially in hamstring and gastrocnemius muscles (Fig 1). Facioscapulohumeral muscular dystrophy was initially suspected, but genetic analysis revealed a normal *Eco*RI fragment size on chromosome 4q35. Her muscle weakness rapidly worsened, and she became wheelchair bound 3 months after her hospitalization. Oral administration of prednisone (1 mg/kg per day) was initiated 10 months after the disease onset, but no improvement in muscle strength was noted, although serum the CK level was decreased to 743 IU/L. In the following 2 years, methotrexate, cyclophosphamide, and tacrolimus were alternately prescribed, leading to normalization of the serum CK levels, but there was only minimal improvement in muscle strength.

Histologic analyses of muscle

Muscle biopsy was performed on the biceps brachii in both patients (Table 1). In patient 1, routine histochemistry revealed moderate fiber size variation, scattered necrotic and regeneration fibers, and minimal endomysial fibrosis (Fig 2). Neither lymphocyte infiltration nor perifascicular atrophy was observed in either patient.

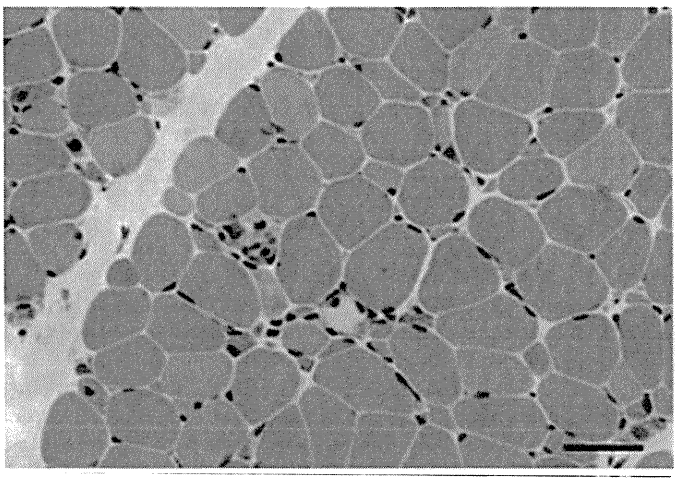

Figure 2. Muscle pathology in patient 1. There are scattered necrotic and regenerating fibers, in addition to moderate fiber size variation and mild endomysial fibrosis on hematoxylin and eosin staining. No lymphocyte infiltration is present. Bars = 50 μm.

On immunohistochemistry, dystrophin, α- to δ-sarcoglycans, α- and β-dystroglycans, dysferlin, caveolin-3, laminin α2, and collagen VI were normally present in the sarcolemma. Major histocompatibility complex class I antigen was only mildly expressed in the membrane in both patients. In addition, it was mildly expressed in the cytoplasm of some fibers in patient 2. Membrane attack complex (C5b-9) was detected in the membrane of only a few muscle fibers and in some capillaries in both patients.

Anti-SRP antibody assay

We performed an RNA immunoprecipitation assay, which can detect various autoantigens, as previously described [5]. Anti-SRP antibodies were confirmed in all sera obtained from both patients. In contrast, other myositis-specific autoantibodies, including Jo-1, PL-7, PL-12, EJ, OJ, and KS, were negative.

Discussion

In both patients, muscle weakness and atrophy were prominent in the proximal limbs and trunk with marked elevation of the serum CK level on the first examination. Weakness seemed to be chronic at disease onset but rapidly progressive, with the result that both patients became unable to walk independently within 1-2 years from the onset of symptoms. Muscle computed tomography demonstrated atrophy in the trunk and proximal limb muscles from the early stage. Muscle pathology revealed active necrotic and regenerating processes with mild endomysial fibrosis, but no inflammatory infiltrates or perivascular cuffing were observed. In addition, there were no abnormal findings of blood inflammatory markers in both patients. All these clinical and pathologic features indicate the possibility of muscular dystrophy. In fact, facioscapulohumeral muscular dystrophy was initially suspected in patient 2

Table 1. Histologic findings of 2 children with anti-signal recognition particle myopathy

Characteristic	Patient 1	Patient 2
Age at biopsy	6 yr 5 mo	10 yr 4 mo
Necrotic and regenerating fibers	Scattered	Scattered
Fiber size variation	Moderate	Marked
Endomysial fibrosis	Minimal	Mild
Adipose tissue infiltration	None	None
Lymphocyte infiltration	None	None
Perifascicular atrophy	None	None
Major histocompatibility complex class I antigen	Mildly positive, sarcolemma	Mildly positive, sarcolemma; cytoplasm of some fibers
Membrane attack complex	Positive, sarcolemma of a few fibers; some capillaries	Positive, sarcolemma of a few fibers; some capillaries

as a result of asymmetric muscle involvement and prominent shoulder girdle weakness, even though the facial muscles were spared.

The mean age at disease onset in adult patients with anti-SRP myopathy ranges 36-51 years, and adult patients occasionally have systemic inflammatory symptoms such as fever, myalgia, arthritis, Raynaud phenomenon, and skin rashes [6-8,10,12]. On the other hand, Rouster-Stevens and Pachman reported 3 juvenile polymyositis patients with anti-SRP antibody. These African American girls, whose ages ranged 11-16 years, developed muscle weakness immediately after an infection in winter [11]. In addition, these patients exhibited variable systemic manifestations, such as cardiac involvement, gastrointestinal dysmotility, intestinal lung disease, arthritis, and Raynaud phenomenon. In fact, the clinical manifestations of the 2 children reported here resembled muscular dystrophy rather than inflammatory myopathy. These results suggest that anti-SRP myopathy in childhood may have 2 phenotypes: myositis with various systemic signs of immune dysregulation, and necrotizing myopathy with a phenotype mimicking muscular dystrophy.

Anti-SRP myopathy should be considered as a differential diagnosis in children who clinically appear with rapid progression of weakness. Anti-SRP antibodies are rarely detected in patients with systemic sclerosis; however, the detection of anti-SRP antibody is useful for different diagnosis of myopathies [5,7]. Prompt antibody detection may be beneficial, as the condition of patients with anti-SRP myopathy can rapidly deteriorate and may often require immunotherapy. Although the improvement of muscle strength is variable upon steroid treatment, prednisone may ameliorate the disease progression and decrease the serum CK level [11,12]. Our patients and juvenile patients with anti-SRP myopathy, however, seemed to experience poorer response to steroid alone as compared to adults [11]; therefore, combination therapy with other immunomodulators may be necessary.

We thank Drs. Hirofumi Komaki (Department of Pediatric Neurology, National Center Hospital of Neurology and Psychiatry) and Hiroaki Umebayashi (Department of General Medicine, Miyagi Children's Hospital) for providing clinical information, Drs. Wen C. Liang and Kanako Goto (Department of Neuromuscular Research, National Institute of Neuroscience, National Center of Neurology and Psychiatry) for data analysis, and Dr. Norihiro Suzuki (Department of Neurology, Keio University School of Medicine) for valuable comments.

This work was supported by a grant from the Japanese Ministry of Education, Science, Sports, and Culture, a research grant on intractable diseases from the Japanese Ministry of Health, Labour, and Welfare, and a Neuroimmunological Disease Research Committee grant from the Japanese Ministry of Health, Labour, and Welfare.

References

[1] Feldman BM, Rider LG, Reed AM, Pachman LM. Juvenile dermatomyositis and other idiopathic inflammatory myopathies of childhood. Lancet 2008;371: 2201–12.

[2] Rider LG. The heterogeneity of juvenile myositis. Autoimmun Rev 2007;6: 241–7.

[3] Gunawardena H, Betteridge ZE, McHugh NJ. Myositis-specific autoantibodies: their clinical and pathogenic significance in disease expression. Rheumatology (Oxford) 2009;48:607–12.

[4] Reeves WH, Nigam SK, Blobel G. Human autoantibodies reactive with the signal-recognition particle. Proc Natl Acad Sci U S A 1986;83:9507–11.

[5] Suzuki S, Satoh T, Sato S, et al. Clinical utility of anti-signal recognition particle antibody in the differential diagnosis of myopathies. Rheumatology (Oxford) 2008;47:1539–42.

[6] Targoff IN, Johnson AE, Miller FW. Antibody to signal recognition particle in polymyositis. Arthritis Rheum 1990;33:1361–70.

[7] Kao AH, Lacomis D, Lucas M, Fertig N, Oddis CV. Anti-signal recognition particle autoantibody in patients with and patients without idiopathic inflammatory myopathy. Arthritis Rheum 2004;50:209–15.

[8] Hengstman GJD, ter Laak HJ, Vree Egberts WT, et al. Anti-signal recognition particle autoantibodies: marker of a necrotizing myopathy. Ann Rheum Dis 2006;65:1635–8.

[9] O'Hanlon TP, Carrick DM, Targoff IN, et al. Immunogenetic risk and protective factors for the idiopathic inflammatory myopathies: distinguish European American patients with different myositis autoantibodies. Medicine 2006;85: 111–27.

[10] Miller T, Al-Lozi MT, Lopate G, Pestronk A. Myopathy with antibodies to the signal recognition particle: clinical and pathological features. J Neurol Neurosurg Psychiatry 2002;73:420–8.

[11] Rouster-Stevens KA, Pachman LM. Autoantibody to signal recognition particle in African American girls with juvenile polymyositis. J Rheumatol 2008;35:927–9.

[12] Dimitri D, Andre C, Roucoules J, Hosseini H, Humbel RL, Authier FJ. Myopathy associated with anti-signal recognition peptide antibodies: clinical heterogeneity contrasts with stereotyped histopathology. Muscle Nerve 2007;35: 389–95.

Human Molecular Genetics, 2011, Vol. 20, No. 19 **3841–3851**
doi:10.1093/hmg/ddr305
Advance Access published on July 12, 2011

Muscle choline kinase beta defect causes mitochondrial dysfunction and increased mitophagy

Satomi Mitsuhashi[1], Hideyuki Hatakeyama[2], Minako Karahashi[3], Tomoko Koumura[3], Ikuya Nonaka[1], Yukiko K. Hayashi[1], Satoru Noguchi[1], Roger B. Sher[4], Yasuhito Nakagawa[3], Giovanni Manfredi[5], Yu-ichi Goto[2], Gregory A. Cox[4] and Ichizo Nishino[1,*]

[1]Department of Neuromuscular Research and [2]Department of Mental Retardation and Birth Defect Research, National Institute of Neuroscience, National Center of Neurology and Psychiatry, Tokyo, Japan, [3]School of Pharmaceutical Sciences, Kitasato University, Tokyo, Japan, [4]The Jackson Laboratory, Bar Harbor, ME, USA and [5]Weil Medical College of Cornell University, New York, NY, USA

Received May 17, 2011; Revised and Accepted July 7, 2011

Choline kinase is the first step enzyme for phosphatidylcholine (PC) *de novo* biosynthesis. Loss of choline kinase activity in muscle causes rostrocaudal muscular dystrophy (*rmd*) in mouse and congenital muscular dystrophy in human, characterized by distinct mitochondrial morphological abnormalities. We performed biochemical and pathological analyses on skeletal muscle mitochondria from *rmd* mice. No mitochondria were found in the center of muscle fibers, while those located at the periphery of the fibers were significantly enlarged. Muscle mitochondria in *rmd* mice exhibited significantly decreased PC levels, impaired respiratory chain enzyme activities, decreased mitochondrial ATP synthesis, decreased coenzyme Q and increased superoxide production. Electron microscopy showed the selective autophagic elimination of mitochondria in *rmd* muscle. Molecular markers of mitophagy, including Parkin, PINK1, LC3, polyubiquitin and p62, were localized to mitochondria of *rmd* muscle. Quantitative analysis shows that the number of mitochondria in muscle fibers and mitochondrial DNA copy number were decreased. We demonstrated that the genetic defect in choline kinase in muscle results in mitochondrial dysfunction and subsequent mitochondrial loss through enhanced activation of mitophagy. These findings provide a first evidence for a pathomechanistic link between *de novo* PC biosynthesis and mitochondrial abnormality.

INTRODUCTION

Phosphatidylcholine (PC) is the major phospholipid in eukaryotic cell membranes. Disruption of PC synthesis by loss-of-function mutations in *CHKB* (GenBank Gene ID 1120), which encodes the primary choline kinase isoform in muscle, causes autosomal recessive congenital muscular dystrophy with mitochondrial structural abnormalities in human (1). Loss-of-function mutation in the murine ortholog, *Chkb*, is reported to cause rostrocaudal muscular dystrophy (*rmd*) in the laboratory mouse (2). *Rmd* is so-named because of a gradient of severity of muscle damage—hindlimbs (caudal) are affected more severely than forelimbs (rostral). The most outstanding feature of the muscle pathology in both human patients and *rmd* mice is a peculiar mitochondrial abnormality—mitochondria are greatly enlarged at the periphery of the fiber and absent from the center.

Mitochondria have a variety of cellular functions from energy production to triggering apoptotic cell death (3,4). Inhibition of mitochondrial respiration [chemically or by mitochondrial DNA (mDNA) mutations], disruption of inner membrane potential, senescence and enhanced reactive oxygen species (ROS) production are all known to cause mitochondrial morphological abnormalities (5–8). Conversely,

*To whom correspondence should be addressed at: Department of Neuromuscular Research, National Institute of Neuroscience, National Center of Neurology and Psychiatry, 4-1-1 Ogawahigashi-cho, Kodaira, Tokyo 187-8502, Japan. Tel: +81 423461712; Fax: +81 423461742; Email: nishino@ncnp.go.jp

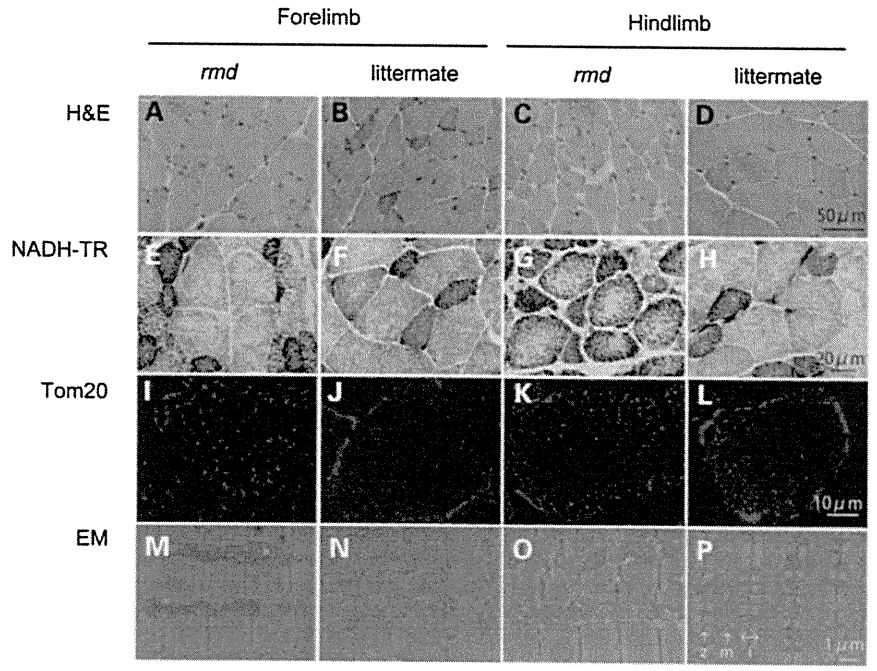

Figure 1. Muscle histopathology. H&E staining of triceps or quadriceps femoris muscles in 8-week-old homozygous *rmd* mutant mice and unaffected (+/*rmd* or +/+) littermate controls (**A**–**D**) shows dystrophic changes including variation in fiber size, necrosis and regeneration of individual fibers and interstitial fibrosis. NADH-TR staining (**E**–**H**), immunostaining of mitochondrial outer membrane protein Tom20 and EM (**M**–**P**) show abnormal mitochondria. Mitochondria in *rmd* muscle fibers are enlarged and prominent at the periphery, but sparse in the center (**I**–**L**). z, Z line; m, M line; i, I band.

primary mitochondrial morphological changes can subsequently cause mitochondrial and cellular dysfunction. Mitochondria are dynamic organelles, which continuously fuse and divide. Disequilibrium of mitochondrial fusion and fission can cause alterations of mitochondrial morphology with mitochondrial dysfunction (9,10). Thus, mitochondrial function and morphology are tightly linked.

It has been reported that mitochondria in *rmd* show decreased membrane potential (11). However, there have been no further studies about mitochondrial functional abnormalities in *rmd*, although its morphology is the most distinct feature compared with other myopathies. In addition, there has been no study about mitochondrial function when PC synthesis is blocked *in vivo*, although mitochondrial respiratory enzyme activities are dependent on membrane phospholipids (12). We hypothesized that the mitochondrial morphological abnormality in *rmd* muscle indicates the presence of a bioenergetic dysfunction caused by mitochondrial membrane phospholipid alteration.

In this study, we demonstrate that mitochondria in *rmd* mouse muscle show reduced PC level, bioenergetic dysfunction and increased ROS production are ubiquitinated and eliminated via mitophagy, leading to the peculiar mitochondrial loss in the skeletal muscle. These findings provide further evidence that mitochondrial dysfunction is related to phospholipid metabolism and may play a role in the pathogenesis of muscle disease.

RESULTS

Light microscopic examination of H&E-stained samples from 8-week-old homozygous *rmd* mutant mice and littermate controls confirmed dystrophic muscle pathology, especially in hindlimb muscles, as previously described (2) (Fig. 1A–D). NADH-TR and immunohistochemistry for mitochondrial outer membrane protein Tom20 also showed that mitochondria were sparse in the muscle fiber both in forelimb and hindlimb muscles of *rmd* mice, while the remaining mitochondria were prominent (Fig. 1E–L). More striking is the mitochondrial enlargement observed by EM (Fig. 1M–P). Mitochondria were rounder and massively enlarged compared with littermate controls. Normally, two mitochondria are present in almost all intermyofibrillar spaces and extend alongside the region between Z band and I bands. In muscles of *rmd* mice, mitochondria were larger than the size of the Z-I length itself, and often exceeded the size of a single sarcomere. In addition, mitochondria were seen only in some intermyofibrillar spaces leaving many regions devoid of mitochondria.

We hypothesized that the abnormal mitochondrial morphology in *rmd* skeletal muscles reflects altered PC content in mitochondrial membranes, as these mitochondria lack the PC biosynthetic pathway. We therefore measured PC, PE and CL in isolated mitochondria (Fig. 2). PE is the second most abundant phospholipid in mitochondria and CL is a mitochondria-specific phospholipid. PC was significantly decreased to 72% in forelimb and to 61% in hindlimb muscles compared with healthy littermates, while PE levels were unchanged. The PC/PE ratio was decreased, reflecting the PC reduction. This reduction is well correlated with the phospholipid compositional alteration in muscle tissue as previously described (1,2). CL showed only a slight decrease and only in the more severely affected hindlimb muscles.

We speculated that mitochondrial function in *rmd* is altered, and therefore measured respiratory enzyme activity and ATP

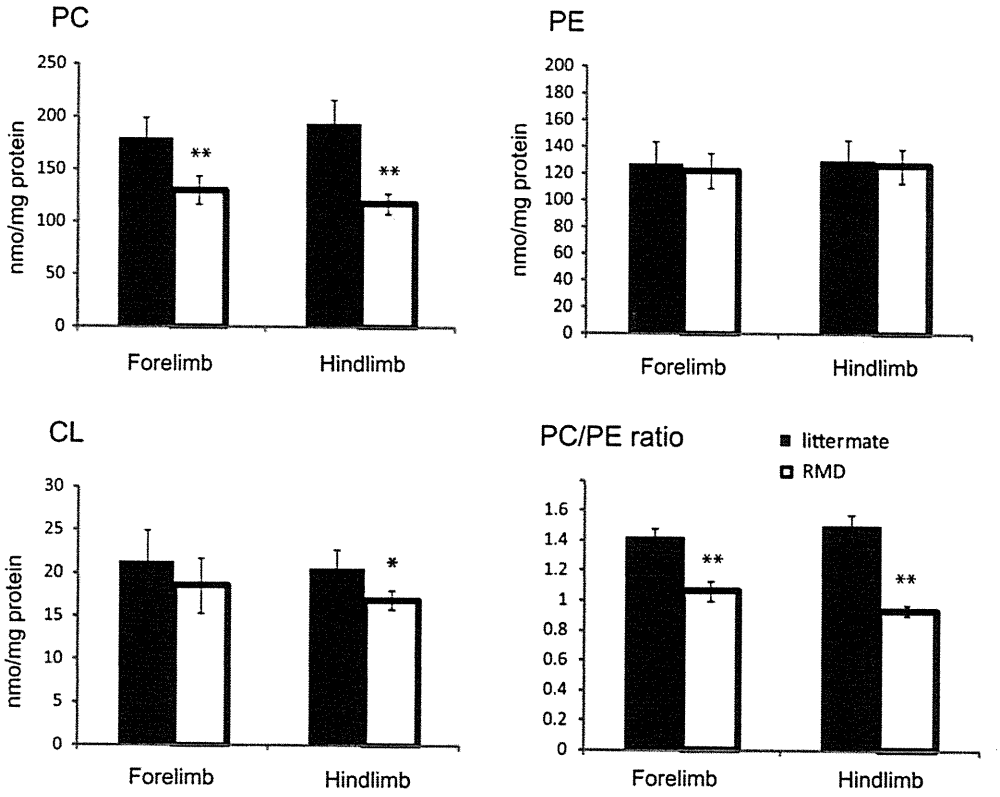

Figure 2. The PC level is decreased in *rmd* muscle mitochondria. The PE level is not altered. The PC/PE ratio is significantly decreased in *rmd*. The CL level is slightly decreased in *rmd* hindlimb. Data are expressed as the mean ± SD of eight experiments. $^{*}P < 0.01$, $^{**}P < 0.0001$.

synthesis in isolated mitochondria in *rmd* muscle. Compared with healthy littermates, only mitochondrial respiratory Complex III activity was significantly decreased in mitochondria from *rmd* forelimb muscles, while Complex I, III and IV activities were significantly decreased in *rmd* hindlimb muscles (Fig. 3A). Mitochondrial ATP synthesis was severely decreased, especially in hindlimb muscles (Fig. 3B), and coenzyme Q9 was moderately decreased in *rmd* compared with littermates (Fig. 3C).

In-gel activity staining on native PAGE showed decreased Complex III activity, especially in hindlimb (Fig. 4A), although normal protein levels of the Complex III were detected by western blot followed by Native PAGE (Fig. 4B). There was no difference in mobility of Complex III in *rmd* and littermate. Furthermore, respiratory chain supercomplex formation, which is important for effective electron transport (24), was not altered in *rmd* (Supplementary Material, Fig. S1).

Mitochondria are a major site of ROS production under normal circumstances and the production of ROS is enhanced when respiration is blocked. To determine whether the identified respiratory defects lead to elevated ROS, we measured superoxide levels from isolated mitochondria. Superoxide production was significantly increased in *rmd* muscle mitochondria, especially in those isolated from the hindlimbs (Fig. 5A). Moreover, the MDA level (Fig. 5B) and 4-hydroxynonenal adducts (Fig. 5C) were increased in *rmd* muscles indicating that oxidative stress is increased in *rmd* muscle.

Interestingly, examination of muscle sections by EM revealed autophagosomes selectively engulfing an entire mitochondrion, without cytoplasm, suggesting that mitophagy is activated in *rmd* skeletal muscles (Fig. 6A). Western blots of isolated mitochondria from muscle showed significantly increased levels of the autophagosome marker LC3 in *rmd* (Fig. 6B). In addition, polyubiquitinated proteins and p62/SQSTM1, which connects ubiquitination and autophagic machineries, were also increased in isolated mitochondria (Fig. 6B). These data suggest that mitochondria are polyubiquitinated and p62 is recruited to mitochondria. We also analyzed PINK1 and the E3 ubiquitin ligase Parkin, which are known to contribute to ubiquitination and mitophagy of damaged mitochondria (25,26). PINK1 and Parkin levels were increased in *rmd* isolated muscle mitochondria (Fig. 6B), suggesting that they were recruited to mitochondria to promote mitophagy. Immunohistochemical analyses demonstrated the colocalization of p62, polyubiquitin and LC3 with mitochondria (Fig. 6C).

We quantified mitochondrial numbers in muscle fibers, mitochondria occupying-area relative to muscle cross-sectional area and mean mitochondrial area in cross-section by morphometric analysis in EM. In *rmd*, the average number of mitochondria per fiber was profoundly decreased (Fig. 7A). However, the average area occupied by mitochondria in each muscle fiber was comparable with littermates (Fig. 7A). This was due to increased mean mitochondrial area in *rmd* (Fig. 7A).

We quantified mtDNA copy number relative to nuclear DNA. In *rmd*, mtDNA was decreased both in forelimb and

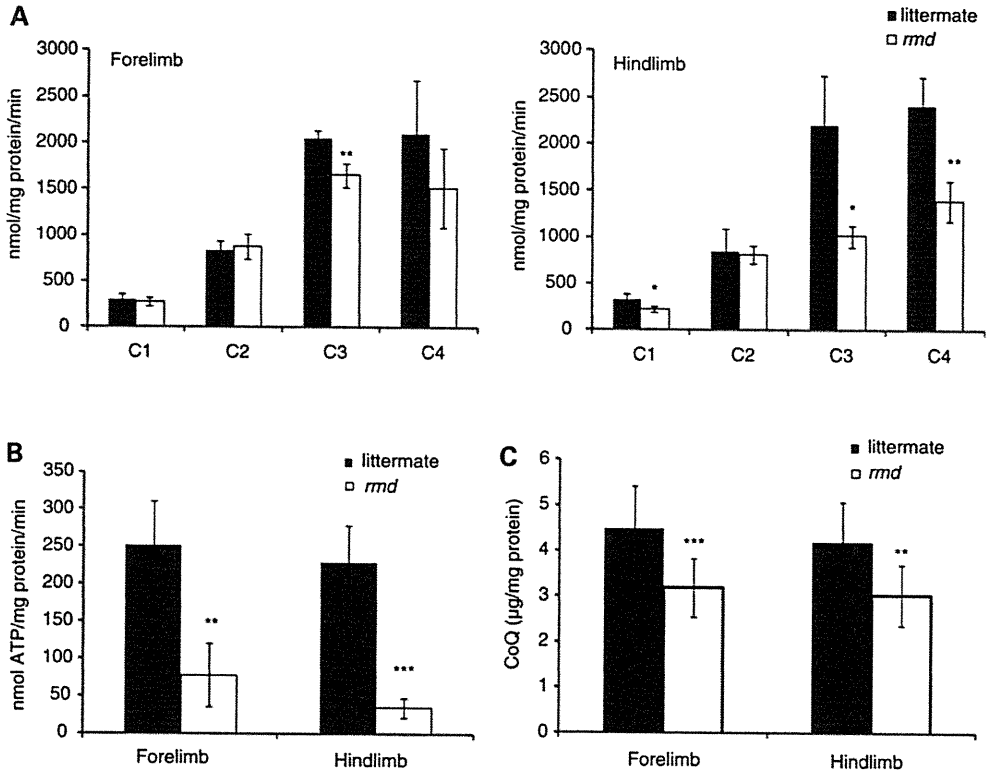

Figure 3. Mitochondrial energetic function is altered and CoQ level is decreased in *rmd*. (**A**) Mitochondrial respiratory chain enzyme activities in *rmd* were compared with healthy littermates. C1, Complex I ; C2, Complex II ; C3, Complex III ; C4, Complex IV ($n = 4$). (**B**) The rate of ATP synthesis measured by luminometry method ($n = 4$). (**C**) Total CoQ9 level (littermate forelimb, $n = 13$; littermate hindlimb, $n = 12$; *rmd* forelimb, $n = 11$; *rmd* hindlimb, $n = 13$). Data are expressed as the mean ± SD of experiment number shown as *n*. $^{*}P < 0.05$, $^{**}P < 0.005$, $^{***}P < 0.001$.

hindlimb muscles compared with littermate controls (Fig. 7B), which was in agreement with the number of mitochondria decrease. The mtDNA copy number in liver is preserved in *rmd*, and reduction in muscle is progressive in age.

DISCUSSION

In the *rmd* mouse, we observed greater superoxide production and more significant Complex III and ATP synthesis deficiencies in hindlimb than in forelimb muscles, correlating with the more severe caudal phenotype. PC was decreased in isolated *rmd* muscle mitochondria as a consequence of disruption of muscle PC biosynthesis because PC cannot be synthesized in mitochondria. This suggests that muscle damage in the *rmd* mouse is primarily due to mitochondrial dysfunction possibly caused by the impaired PC biosynthesis.

Why then are mitochondrial functions altered when PC is decreased? Mitochondria produce energy mainly via oxidative phosphorylation, which transfers electrons by a series of redox reactions through four enzyme complexes, and pumps protons across the mitochondrial inner membrane, producing an electrochemical proton gradient that enables ATP synthesis (3). Here, we demonstrate for the first time a Complex III activity decrease without the loss of the enzyme protein complex in *rmd* muscle mitochondria, suggesting a link between decreased PC content and Complex III activity. One possible explanation is that mitochondrial PC alterations may directly impair Complex III function by affecting lipid–protein interactions (27). PC is a component of the yeast respiratory enzyme complex, as revealed by X-ray crystallography, and thus may regulate enzyme function (28). Alteration of fatty acid composition in PC has been shown to change enzymatic activity in Complexes I, III and IV in a mouse model (29). In this model, Complex III activity is profoundly increased when n-3 fatty acid is increased. In *rmd*, it is reported that docosahexiaenoic acid containing PC, the major n-3 fatty acid in muscle PC, is profoundly decreased in muscle and in isolated mitochondria (1). This suggests a possible association between phospholipid composition alterations and respiratory chain enzymatic activities due to the choline kinase defect in *rmd* muscle.

Through the oxidative phosphorylation process, ROS are also generated as byproducts even in normal cellular states, but especially when respiration is inhibited (30,31). In *rmd* mouse muscle, ROS production from isolated mitochondria was increased, which may be related to the respiratory chain defect caused by PC reduction in mitochondria. Interestingly, selenium-deficient myopathy is associated with muscle pathology showing similar enlarged and sparse mitochondrial morphological abnormalities to the *rmd* mice and the human congenital muscular dystrophy caused by *CHKB* mutations (32). As selenium is a cofactor of glutathione peroxidase, selenium deficiency is thought to cause oxidative stress (33,34). Morphological similarity between choline kinase beta deficiency and selenium deficiency suggests that ROS may play a key role in the formation of the mitochondrial

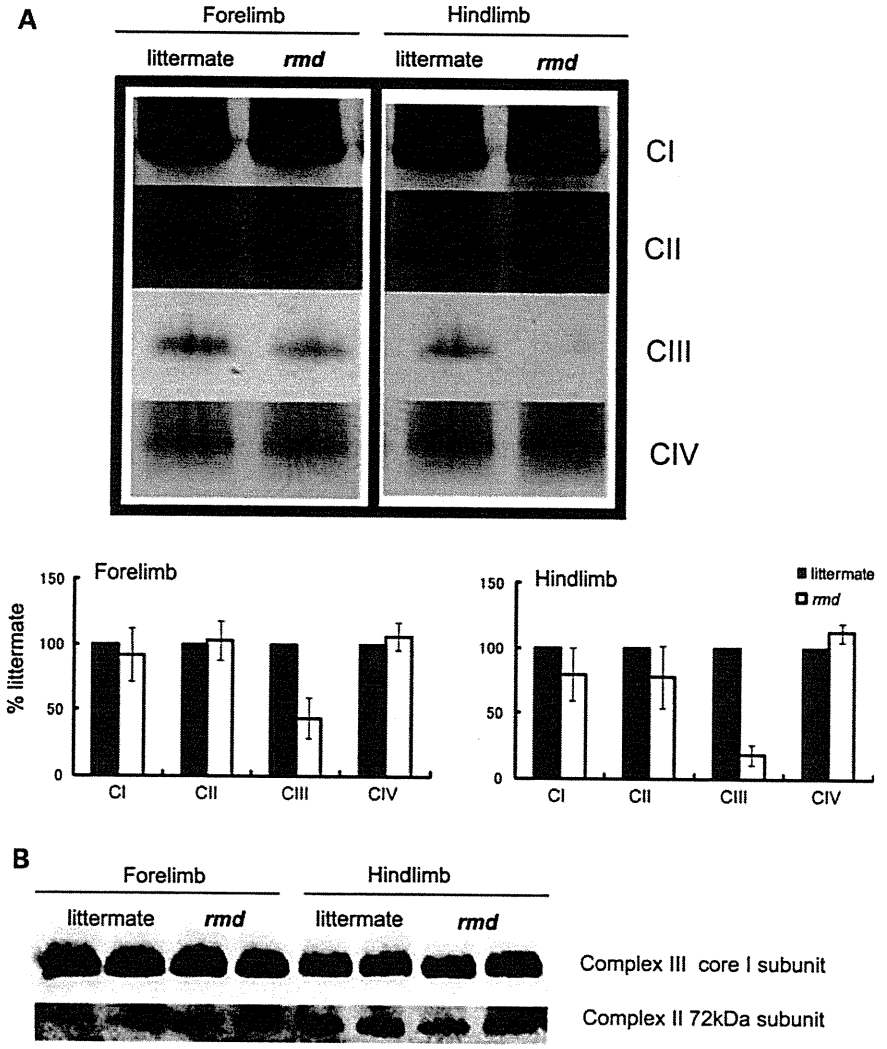

Figure 4. Mitochondrial respiratory enzyme activity is decreased without the loss of the enzyme complex. (**A**) Native PAGE gel electrophoresis. In-gel activity staining shows that Complex III activity is decreased in *rmd*. Representative data from four different experiments are shown. (**B**) Immunoblotting of Complex II and III shows protein levels are maintained despite defect in significant Complex III enzymatic activity. Representative data from three different experiments of six samples are shown.

abnormalities in *rmd* myopathy. In another model, depletion of glutathione, which provides cells with a reducing environment and detoxifies the ROS, is reported to cause mitochondria enlargement in muscle, also suggesting the possible link between mitochondrial enlargement and ROS in skeletal muscle (35).

In addition, as a major site of ROS production, mitochondria themselves are prone to ROS damage (36). Recent studies have shown that damaged mitochondria are eliminated by selective autophagy, called mitophagy, most likely as a quality control mechanism to protect the cells (37,38). In addition to mitochondrial enlargement, we observed large areas devoid of mitochondria. Mitochondrial depolarization can trigger mitophagy in cell culture models (26). PINK1 and Parkin interactions promote ubiquitination of mitochondrial outer membrane proteins, and induce mitophagy. This process is mediated by p62, an adaptor molecule, which interacts directly with ubiquitin and LC3 (25,39). ROS generated from mitochondria are also important for mitophagy (39). Interestingly, we found increased mitophagy in *rmd*, accompanied by mitochondrial ubiquitination and recruitment of p62 and LC3. Enhanced PINK1 and Parkin expression in mitochondria likely reflects the process of elimination of damaged mitochondria as a consequence of mitochondrial dysfunction and ROS production. These findings were similar to those in cells treated with the protonophore carbonyl cyanide m-chlorophenyl hydrazone (CCCP) or respiratory chain inhibitors (25,26). In *rmd*, decreased membrane potential (11), as a consequence of respiratory chain insufficiency and ROS production, may trigger mitophagy and thus increased mitochondrial clearance, which may lead to energy crisis and result in cell death and muscular dystrophy.

We observed progressive loss of mtDNA with age, together with progressive loss of mitochondria. We suggest that mtDNA depletion in this case results from increased mitophagy, because mtDNA is known to be degraded by mitophagy in cultured hepatocytes (40) and because the pathological features of CHKB-deficient myopathy are clearly distinct from those

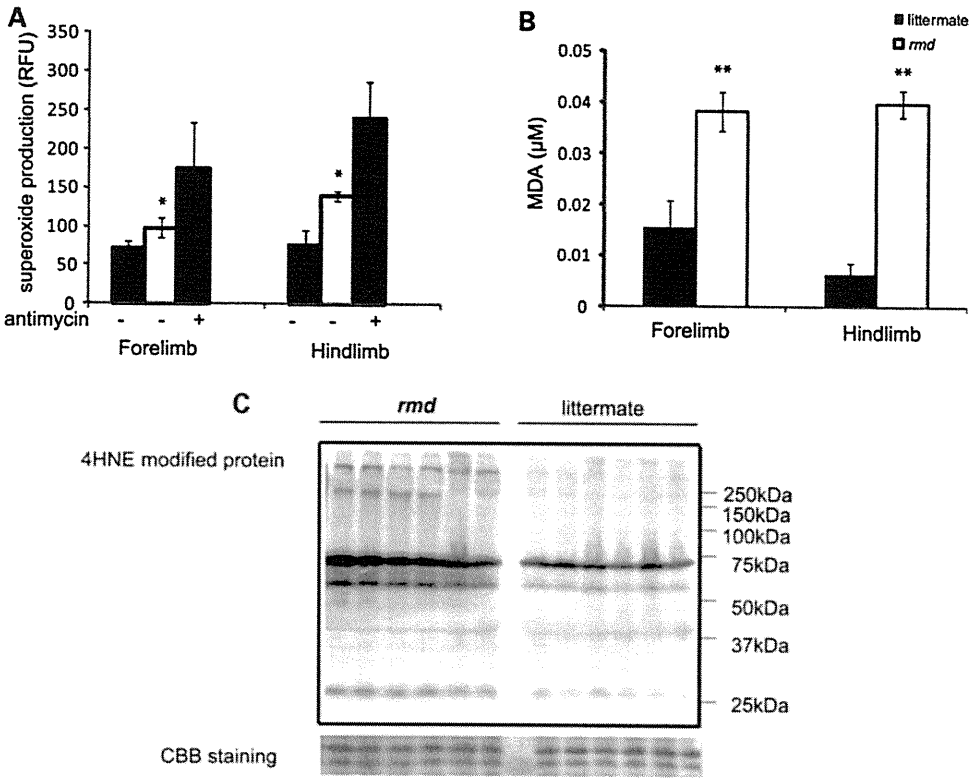

Figure 5. Mitochondrial superoxide production is increased and oxidative stress is increased in muscle tissue in *rmd*. (**A**) Mitochondrial superoxide production is enhanced in *rmd*, especially in hindlimb muscle mitochondria. Data are shown as the mean ± SD of seven experiments. $^{*}P < 0.001$. (**B**) MDA levels are increased in muscle tissue. $^{**}P < 0.0005$. Data are shown as the mean ± SD ($n = 4$ for *rmd* and $n = 5$ for littermate controls). (**C**) HNE4-modified proteins are increased in *rmd* hindlimb muscle. Coomassie brilliant blue staining is shown as a loading control. Representative data of six samples.

observed in 'primary' mtDNA depletion syndromes, usually associated with defective mtDNA synthesis, in which muscle fiber mitochondria are increased both in number and size, causing the 'ragged-red fiber' appearance (41).

In summary, we have demonstrated for the first time a pathogenic mechanism that links PC reduction in the mitochondrial membranes of *rmd* muscle to mitochondrial morphological and functional abnormalities and the induction of mitophagy as a response to structural and functional damage by ROS generation or impaired bioenergetics. These findings indicate the importance of PC *de novo* synthesis pathway and phospholipid composition of mitochondrial membrane in the maintenance of mitochondria and muscle.

MATERIALS AND METHODS

Rmd mice

Eight-week-old *rmd* mice (2) were used for all analysis and were compared with healthy littermates. The Ethical Review Committee on the Care and Use of Rodents in the National Institute of Neuroscience, National Center of Neurology and Psychiatry approved all mouse experiments.

Histological analyses

The quadriceps femoris muscles were freeze-fixed in liquid-nitrogen-cooled isopentane and stored at −80°C. Serial transverse sections of 10 μm thickness were stained with a series of histochemical methods, including hematoxylin and eosin (H&E) and nicotine amide adenine dinucleotide-tetrazolium reductase (NADH-TR), as previously described (13), and were observed by light microscopy.

Immunohistochemical analyses were performed as previously described (13). Briefly, 6 μm thick frozen muscle sections were fixed in cold acetone for 5 min. After blocking with 5% normal goat serum, sections were incubated with primary antibodies for 2 h at 37°C. After rinses with phosphate-buffered saline, sections were incubated with secondary Alexa Fluor 488- or Alexa Fluor 568-labeled goat anti-mouse

Figure 6. Mitochondrial degeneration in *rmd*. (**A**) EM of extensor digitorum longus muscle. In *rmd*, mitochondria are degraded by mitophagy. Scale bar = 0.5 μm. (**B**) Western blot of isolated muscle mitochondria immunodetected for Parkin, polyubiquitin, p62/SQSTM1 and LC3. TOM20, a mitochondrial outer membrane protein is used as loading control. Hindlimb mitochondria in *rmd* show significantly increased expression level in these mitophagy markers. (**C**) p62 and TOM20 immunohistrochemistry of hindlimb muscle section. Note that mitochondria are significantly enlarged and sparse in *rmd*. p62 colocalizes with the mitochondrial outer membrane protein TOM20. Polyubiquitin and mitochondrial protein cytochrome c oxidase (COX) colocalize. LC3 and TOM20 colocalize. Polyubiquitin and p62 colocalize. Scale bar = 10 μm.

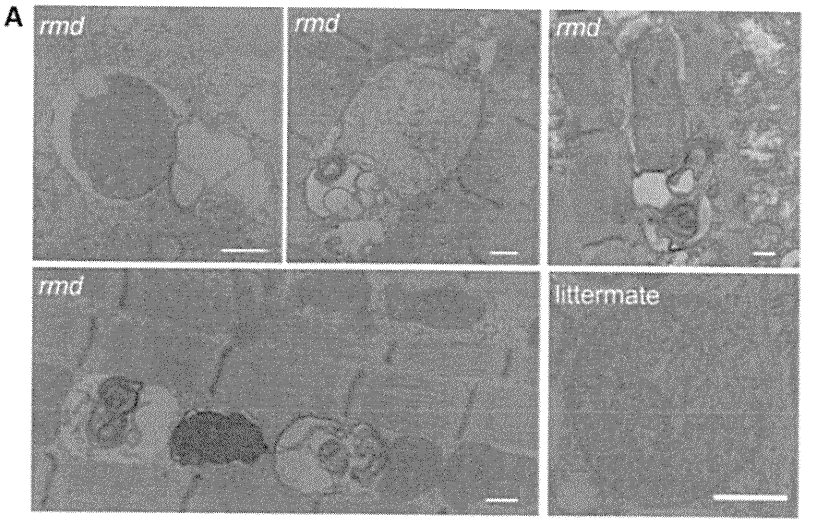
A
rmd
rmd
rmd
rmd
littermate

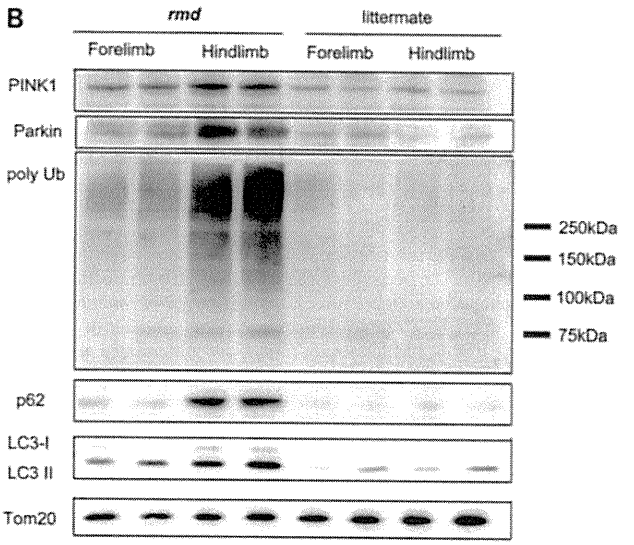
B
rmd
littermate
Forelimb
Hindlimb
Forelimb
Hindlimb
PINK1
Parkin
poly Ub
250kDa
150kDa
100kDa
75kDa
p62
LC3-I
LC3 II
Tom20

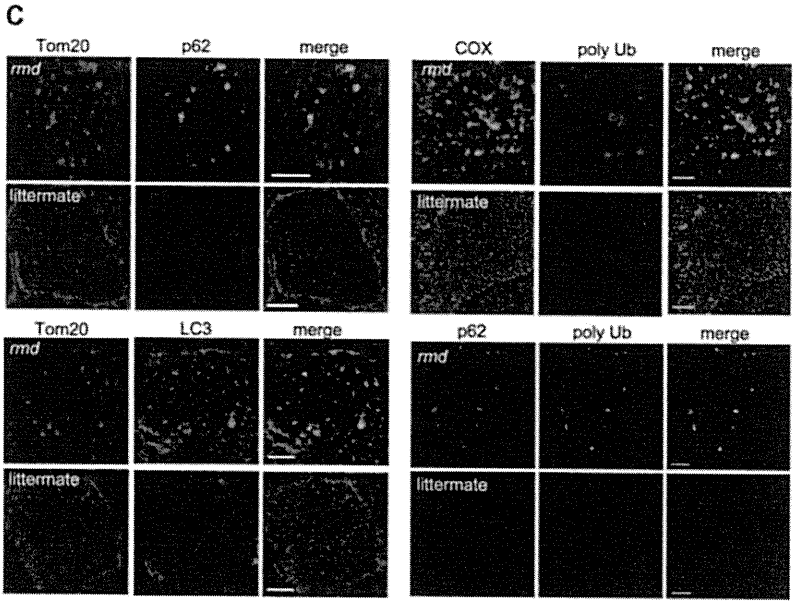
C
Tom20
p62
merge
COX
poly Ub
merge
rmd
littermate
Tom20
LC3
merge
p62
poly Ub
merge
rmd
littermate

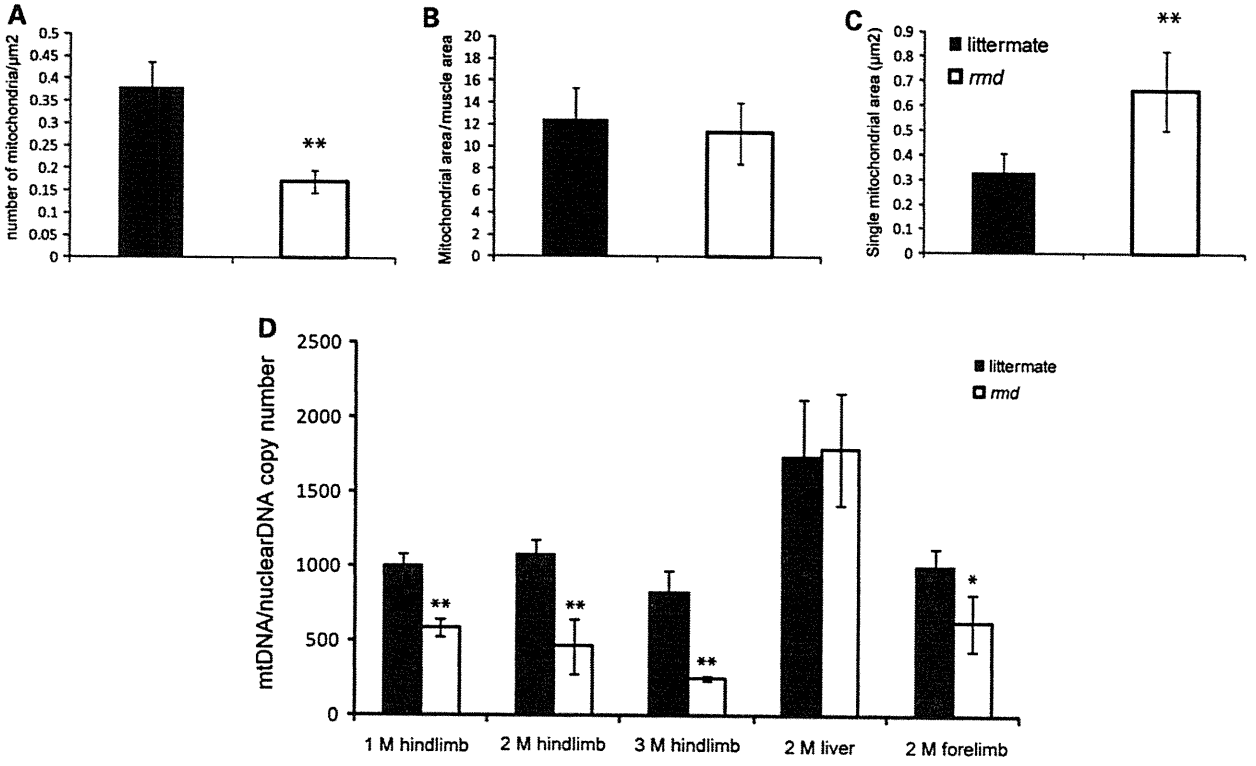

Figure 7. (**A**) Mitochondrial morphometrical analysis. All mitochondria are counted in cross-sections of EDL muscle by EM. Number of mitochondria per 1 μm^2 of muscle fiber cross-sectional area is shown ($n = 20$). The percentage of area occupied by mitochondria in a cross-section of muscle fiber is not different in *rmd* and littermates ($n = 20$). The average total mitochondrial area per muscle fiber is larger in *rmd* compared with littermates ($n = 20$). $^*P < 0.005$, $^{**}P < 0.0005$. (**B**) mtDNA copy number is decreased in *rmd* compared with littermate controls. Copy number of mtDNA (ND1) was normalized by nuclear DNA (*pcam1*) (M; month-old, 1 M hindlimb: *rmd*; $n = 4$, littermates; $n = 4$. 2 M hindlimb: *rmd*; $n = 5$, littermates; $n = 6$, 3 M hindlimb: *rmd*; $n = 4$, littermates; $n = 6$. 2 M liver: *rmd*; $n = 5$, littermates; $n = 5$. 2 M forelimb: *rmd*; $n = 6$, littermates; $n = 6$).

or rabbit antibodies at room temperature for 45 min. Confocal images were obtained with FLUOVIEW FV500 systems (Olympus) using a ×100 objective.

For observation by electron microscopy (EM), muscle samples were fixed in 2.5% glutaraldehyde in 0.1 M cacodylate buffer. Specimens were post-fixed in 1% osmium tetroxide in the same buffer, dehydrated with graded series of ethanol and embedded in epon, as previously described (13). Ultrathin sections were stained with uranyl acetate and lead citrated, and were analyzed by a FEI Tecnai Spirit at 120 kV.

Isolation of skeletal muscle mitochondria

Mitochondria from skeletal muscle of whole forelimb and hindlimbs were isolated by differential centrifugation. Fresh muscle was minced and homogenized using a motor-driven Teflon pestle homogenizer with ice-cold mitochondrial isolation buffer [10 mM Tris–HCl pH 7.2, 320 mM sucrose, 1 mM ethylenediaminetetraacetic acid, 1 mM dithiothreitol, 1 mg/ml bovine serum albumin (BSA)] and centrifuged at 1500*g* for 5 min. Supernatant fraction was centrifuged at 15 000*g* for 20 min, and the pellet was resuspended in mitochondrial isolation buffer. The centrifugation was repeated twice. Protein concentration was determined by the Bradford method using Bio-Rad Protein Assay (Bio-Rad Laboratories), according to the manufacturer's protocol.

Lipid extraction, phospholipid separation and determination

PC, phosphatidylethanolamine (PE) and cardiolipin (CL) were extracted from isolated mitochondria of forelimb and hindlimb muscles, separated by one-dimensional thin layer chromatography (TLC) and amount of each phospholipid was measured by phosphorus analysis (14,15). Briefly, total lipids in frozen muscle biopsy samples were extracted according to the method of Bligh and Dyer (14). Each extract was evaporated to dryness under nitrogen, and the residues were then dissolved in a small amount of a 2:1 v/v mixture of chloroform and methanol and applied to a TLC plate (Merck, Silica Gel 60). The plate was developed with a medium of chloroform:-methanol:formic acid:acetic acid = 100:100:9:9 (v/v/v/v). The products and standards were visualized with primulin reagent, and the products identified by comparison with chromatographic standards. PC and PE were then scraped from the TLC plate for quantification. Phospholipids were quantified according to the method of Rouser *et al.* (15). Briefly, the lipids were digested by heating for 1 h at 200°C with 70% perchloric acid. After cooling, ammonium molybdate and ascorbic acid solution were added in that order. Color was developed after heating for 5 min in a boiling water bath. Absorbance was determined at 820 nm by spectrophotometer. Phospholipid levels were corrected by the total protein amount in isolated mitochondria.

Respiratory enzyme activity and ATP synthesis

Mitochondrial respiratory enzyme activities were measured as previously described, using colorimetric assays in isolated mitochondria (16,17). Complex I (NADH-ubiquinone oxidoreductase) activity was measured by the reduction of 10 μM decylubiquinone (DB) in the presence of 2 mM potassium cyanide (KCN), 50 μg/ml antimycin and 50 μM NADH at 272 nm. Complex II (succinate-ubiquinone oxidoreductase) activity was measured by the reduction of 50 μM 2,6-dichlorophenolindophenol in the presence of 20 mM succinate, 2.5 μg/ml rotenone, 2.5 μg/ml antimycin, 2 mM KCN and 50 μM DB at 600 nm. Complex III (ubiquinol-ferricytochrome c oxidoreductase) activity was measured by the reduction of 50 μM cytochrome c at 550 nm in the presence of 50 μM reduced DB and 2 mM KCN. Complex IV (ferrocytochrome c-oxigen oxidoreductase) activity was measured by the oxidation of 2.5 μM reduced cytochrome c at 550 nm. The activity was calculated using an extinction coefficient of 8 mM^{-1} cm^{-1}, 19.1 mM^{-1} cm^{-1}, 19.0 mM^{-1} cm^{-1} and 19.0 mM^{-1} cm^{-1} for Complexes I, II, III and IV, respectively. The specific activity of the enzymes was expressed as nmol of each substrate oxidized or reduced/min/mg of mitochondrial protein.

Mitochondrial ATP synthesis was measured by the method of Manfredi and colleagues (18). Briefly, isolated mitochondria were resuspended in 0.25 M sucrose, 50 mM 4-(2-hydroxyethyl)-1-piperazineethanesulfonic acid (HEPES), 2 mM $MgCl_2$, 1 mM ethylene glycol tetraacetic acid (EGTA) and 10 mM KH_2PO_4, pH 7.4. Then 0.15 mM P1,P5-di(adenosine) pentaphosphate, 1 mM malate, 1 mM pyruvate, luciferin and luciferase and 0.1 mM adenosine diphosphate (ADP) were added, and light emission was recorded by luminometer. For each sample, 1 mM oligomycin-added sample was used to obtain the baseline luminescence corresponding to non-mitochondrial ATP production.

CoQ9 determination

Total CoQ9 contents in isolated mitochondria were analyzed with high performance liquid chromatography (HPLC) by electrochemical detection according to the standard procedure described by Tang *et al.* (19). Briefly, isolated muscle mitochondria pellet were lysed with 2-propanol, vortexed for 1 min and centrifuged at 2000*g* for 10 min and then clear supernatant was applied for HPLC Coul Array Detector Model 5600A (ESA BIOSCIENCES, Inc.) with Capcell Pak C18 MG 100 column (3.2 I.D × 150 mm length; ESA BIOSCIENCES, Inc.). The mobile phase was degassed methanol containing 0.4% sodium acetate, 1.5% acetic acid, 1% 2-propanol and 8% n-hexane. Chromatographic data were analyzed with CoulArray Data Station 3.00 (ESA Biosciences). Standard curves were created with both oxidized and reduced CoQ9. Total CoQ9 level was determined according to the standard curve and corrected by the total protein level in isolated mitochondria as measured by the Bradford method.

High-resolution clear native PAGE

High-resolution clear native polyacrylamide gel electrophoresis (PAGE) was performed by the method of Wittig *et al.* (20). Briefly, isolated mitochondria were solubilized with Native PAGE Sample buffer (Invitrogen) containing 0.3% n-dodecyl-β-D-maltoside (Dojindo). Twenty micrograms of protein were applied to 3–12% NativePAGE Bis–Tris gel (Invitrogen). Native PAGE buffer (Invitrogen) was used for anode buffer and Native PAGE buffer containing 0.02% n-dodecyl-β-D-maltoside and 0.05% deoxycolate was used for cathode buffer.

For in-gel catalytic activity assays, gels were incubated in the following solutions: Complex I, 5 mM Tris–HCl pH 7.4, 140 μM NADH and 3 mM nitro tetrazolium blue (NTB); Complex II, 5 mM Tris–HCl pH 7.4, 20 mM succinate, 3 mM NTB and 200 μM phenazine methosulfate; Complex III, 50 mM sodium phosphate buffer pH 7.2 and 0.5 mg/ml diaminobenzidine (DAB); Complex IV, 50 mM sodium phosphate buffer (pH 7.2), 0.5 mg/ml DAB and 5 mM cytochrome c.

For immunoblotting, gels were incubated for 20 min in 300 mM Tris, 100 mM acetic acid, 1% sodium dodecyl sulfate (SDS), pH 8.6 and then electroblotted to polyvinylidene fluoride (PVDF) membrane (Millipore). Complexes II and III were detected with monoclonal antibodies against the 70 kDa subunit (Abcam) and core 2 subunit (Invitrogen), respectively.

Measurement of mitochondrial superoxide (O_2^-) production

Mitochondrial superoxide production was measured by dehydroethidium (DHE) (Molecular Probes), as described previously (21). Isolated mitochondria were incubated with 200 mM mannitol, 70 mM sucrose, 2 mM HEPES pH 7.4, 0.5 mM EGTA and 0.1% BSA. Reagents were added in the following order: 1 mM glutamate, 1 mM malate, 1 μM DHE, 0.25 mM ADP and 5 mM KH_2PO_4. Fluoresence was measured by Cytofluor 4000 (Applied biosystems) at excitation/emission = 530/620 nm.

Measurement of malondialdehyde in muscle

Malondialdehyde (MDA) levels were measured in muscle homogenates using an LPO-485 assay kit (BIOXYTEC), according to the manufacturer's protocol.

Western blot analysis for muscle tissue and isolated mitochondria

Proteins were extracted from quadriceps femoris muscles or mitochondria isolated from forelimb and hindlimb muscles and suspended in SDS sample buffer; 125 mM Tris–HCl pH 6.8, 5% β-mercaptoethanol, 2% SDS and 10% glycerol. Extracted proteins were separated on acrylamide gels, and then transferred onto PVDF membranes (Millipore). Blocking solution of 5% skim milk was used. ImageQuant LAS 4000 Mini Biomolecular Imager (GE Healthcare) was used for evaluating bands.

Quantification of mtDNA by real-time PCR

Total DNA was isolated from triceps and quadriceps femoris and liver by proteinase K digestion and standard phenol–chloroform

extraction. Copy number of mtDNA (ND1) was quantified by real-time polymerase chain reaction (PCR) using SYBR Green PCR Kit (Qiagen) with *pcam1* as the control for the nuclear genome copy number. We used the following primers: ND1 forward primer, CCTATCACCCTTGCCATCAT; ND1 reverse primer, GAGGCTGTTGCTTGTGTGAC; *pcam1* DNA forward primer, ATGGAAAGCCTGCCATCATG; *pcam1* DNA reverse primer, TCCTTGTTGTTCAGCATCAC.

The amount of mtDNA relative to nuclear DNA was calculated using the following formula: mtDNA/nuclear DNA $= 2^{-(Ct_{mtDNA}-Ct_{nuclerDNA})}$ where Ct is the threshold cycle (22).

Morphometrical analysis of mitochondria

Cross-sectional EM image of extensor digitorum longus (EDL) muscle from *rmd* and littermates was analyzed by Image J software (23). Total areas of all mitochondria in 20 muscle fibers were calculated and compared with cross-sectional fiber areas. Total number of mitochondria per muscle fiber was counted.

Antibodies

Primary antibodies used were: mouse anti-4-hydroxy-2-nonenal (4-HNE) modified protein antibody (HNEJ-2,JalCA), rabbit anti-PINK1 antibody (BC100-494, Novus Biologicals), mouse anti-Parkin antibody (4211, Cell Signaling), rabbit anti-p62/SQSTM1 antibody (PWS860, Biomol), rabbit anti-LC3 antibody (NB100-2220, Novus Biologicals), mouse anti-poly-ubiquitin antibody (FK1, Biomol), rabbit anti-TOM20 antibody (FL-145, Santa Cruz), mouse anti-COX subunit 1 antibody (Invitrogen) and mouse anti-VDAC antibody (20B12, Santa Cruz). Second antibodies used were: horse radish peroxidase-labeled goat anti-mouse (Beckman Coulter) or rabbit antibodies (Cell Signaling), Alexa Fluor 488- and Alexa Fluor 568-labeled goat anti-mouse or rabbit antibodies (Invitrogen).

Statistical analysis

Data are presented as mean ± SD. Mean differences were compared with the analysis of *t*-test using R software version 2.11.0 (http://www.r-project.org/).

SUPPLEMENTARY MATERIAL

Supplementary Material is available at *HMG* online.

ACKNOWLEDGEMENTS

We thank Megumu Ogawa, Kanako Goto and Junko Takei for technical assistance.

FUNDING

This study was supported partly by the Research on Psychiatric and Neurological Diseases and Mental Health of Health and Labour Sciences Research Grants; partly by the Research on Intractable Diseases of Health and Labor Sciences Research Grants; partly by the Research Grant for Nervous and Mental Disorders (20B-12, 20B-13) from the Ministry of Health, Labour and Welfare; partly by an Intramural Research Grant (23-4, 23-5) for Neurological and Psychiatric Disorders from NCNP; partly by KAKENHI (20390250, 22791019); partly by Research on Publicly Essential Drugs and Medical Devices of Health and Labor Sciences Research Grants; partly by the Program for Promotion of Fundamental Studies in Health Sciences of the National Institute of Biomedical Innovation (NIBIO); and partly by the Grant from Japan Foundation for Neuroscience and Mental Health. G.A.C. and R.B.S. were supported in part by a National Institutes of Health Grant (AR054170 to G.A.C.).

REFERENCES

1. Mitsuhashi, S., Ohkuma, A., Talim, B., Karahashi, M., Koumura, T., Aoyama, C., Kurihara, M., Quinlivan, R., Sewry, C., Mitsuhashi, H. *et al.* (2011) A congenital muscular dystrophy with mitochondrial structural abnormalities caused by defective de novo phosphatidylcholine biosynthesis. *Am. J. Hum. Genet.*, **88**, 845–851.
2. Sher, R.B., Aoyama, C., Huebsch, K.A., Ji, S., Kerner, J., Yang, Y., Frankel, W.A., Hoppel, C.A., Wood, P.A., Vance, D.E. *et al.* (2006) A rostrocaudal muscular dystrophy caused by a defect in choline kinase beta, the first enzyme in phosphatidylcholine biosynthesis. *J. Biol. Chem.*, **281**, 4938–4948.
3. Saraste, M. (1999) Oxidative phosphorylation at the fin de siècle. *Science*, **283**, 1488–1493.
4. Spierings, D., McStay, G., Saleh, M., Bender, C., Chipuk, J., Maurer, U. and Green, D.R. (2005) Connected to death: the (unexpurgated) mitochondrial pathway of apoptosis. *Science*, **310**, 66–67.
5. Wakabayashi, T. (2002) Megamitochondria formation—physiology and pathology. *J. Cell Mol. Med.*, **6**, 497–538.
6. Benard, G., Bellance, N., James, D., Parrone, P., Fernandez, H. and Letellier, T. (2007) Mitochondrial bioenergetics and structural network organization. *J. Cell Sci.*, **120**, 838–848.
7. Yoon, Y.S., Yoon, D.S., Lim, I.K., Yoon, S.H., Chung, H.Y., Rojo, M., Malka, F., Jou, M.J., Martinou, J.C. and Yoon, G. (2006) Formation of elongated giant mitochondria in DFO-induced cellular senescence: involvement of enhanced fusion process through modulation of Fis1. *J. Cell Physiol.*, **209**, 468–480.
8. Karbowski, M., Kurono, C., Wozniak, M., Ostrowski, M., Teranishi, M., Nishizawa, Y., Usukura, J., Soji, T. and Wakabayashi, T. (1999) Free radical-induced megamitochondria formation and apoptosis. Free Radic. Biol. Med., **26**, 396–409.
9. Chen, H., Detmer, S.A., Ewald, A.J., Griffin, E.E., Fraser, S.E. and Chan, D.C. (2003) Mitofusins Mfn1 and Mfn2 coordinately regulate mitochondrial fusion and are essential for embryonic development. *J. Cell Biol.*, **160**, 189–200.
10. Chen, H., Chomyn, A. and Chan, D.C. (2005) Disruption of fusion results in mitochondrial heterogeneity and dysfunction. *J. Biol. Chem.*, **280**, 26185–26192.
11. Wu, G., Sher, R.B., Cox, G.A. and Vance, D.E. (2009) Understanding the muscular dystrophy caused by deletion of choline kinase beta in mice. *Biochim. Biophys. Acta*, **1791**, 347–356.
12. Daum, G. (1985) Lipids of mitochondria. *Biochim. Biophys. Acta*, **822**, 1–42.
13. Hayashi, Y.K., Matsuda, C., Ogawa, M., Goto, K., Tominaga, K., Mitsuhashi, S., Park, Y.E., Nonaka, I., Hino-Fukuyo, N., Haginoya, K. *et al.* (2009) Human PTRF mutations cause secondary deficiency of caveolins resulting in muscular dystrophy with generalized lipodystrophy. *J. Clin. Invest.*, **119**, 2623–2633.
14. Bligh, E.G. and Dyer, W.J. (1959) A rapid method of total lipid extraction and purification. *Can. J. Biochem. Physiol.*, **37**, 911–917.
15. Rouser, G., Fkeischer, S. and Yamamoto, A. (1970) Two dimensional then layer chromatographic separation of polar lipids and determination of phospholipids by phosphorus analysis of spots. *Lipids*, **5**, 494–496.
16. Mimaki, M., Hatakeyama, H., Ichiyama, T., Isumi, H., Furukawa, S., Akasaka, M., Kamei, A., Komaki, H., Nishino, I., Nonaka, I. *et al.* (2009)

Different effects of novel mtDNA G3242A and G3244A base changes adjacent to a common A3243G mutation in patients with mitochondrial disorders. *Mitochondrion*, **9**, 115–122.
17. Trounce, I.A., Kim, Y.L., Jun, A.S. and Wallace, D.C. (1996) Assessment of mitochondrial oxidative phosphorylation in patient muscle biopsies, lymphoblasts, and tranmitochondrial cell lines. *Methods enzymol.*, **264**, 484–509.
18. Vives-Bauza, C., Yang, L. and Manfredi, G. *Methods in Cell Biology. Mitochondria*, 2nd edn. Academic Press, London, UK, Vol. 80, Part 2, 7, 155–171.
19. Tang, P.H., Miles, M.V., Miles, L., Quinlan, J., Wong, B., Wenisch, A. and Bove, K. (2004) Measurement of reduced and oxidized coenzyme Q9 and coenzyme Q10 levels in mouse tissues by HPLC with coulometric detection. *Clin. Chim. Acta*, **341**, 173–184.
20. Wittig, I., Karas, M. and Schagger, H. (2007) High resolution clear native electrophoresis for in-gel functional assays and fluorescence studies of membrane protein complexes. *Mol. Cell Proteomics*, **6**, 1215–1225.
21. Armstrong, J.S. and Whiteman, M. *Methods in Cell Biology. Mitochondria*, 2nd edn. Academic Press, London, UK, Vol. 80, 18, 355–377.
22. Naini, A. and Shanske, S. *Methods in Cell Biology. Mitochondria*, 2nd edn. Academic Press, London, UK, Vol. 80, Part2, 22, 448–449.
23. Abramoff, M.D., Magelhaes, P.J. and Ram, S.J. (2004) Image processing with Image J. *Biophotonics Int.*, **11**, 36–42.
24. Zhang, M., Mileykovskaya, E. and Dowhan, W. (2002) Gluing the respiratory chain together. Cardiolipin is required for supercomplex formation in the inner mitochondrial membrane. *J. Biol. Chem.*, **277**, 43553–43556.
25. Geisler, S., Holmström, K.M., Skujat, D., Fiesel, F.C., Rothfuss, O.C., Kahle, P.J. and Springer, W. (2010) PINK1/Parkin-mediated mitophagy is dependent on VDAC1 and p62/SQSTM1. *Nat. Cell Biol.*, **12**, 119–131.
26. Narendra, D., Tanaka, A., Suen, D.F. and Youle, R.J. (2008) Parkin is recruited selectively to impaired mitochondria and promotes their autophagy. *J. Cell Biol.*, **183**, 795–803.
27. Lee, A.G. (2003) Lipid-protein interactions in biological membranes: a structural perspective. *Biochim. Biophys. Acta*, **1612**, 1–40.
28. Lange, C., Nett, J.H., Trumpower, B.L. and Hunte, C. (2001) Specific roles of protein-phospholipid interactions in the yeast cytochrome bc1 complex structure. *EMBO J.*, **20**, 6591–6600.
29. Hagopian, K., Weber, K.L., Hwee, D.T., Van Eenennaam, A.L., López-Lluch, G., Villalba, J.M., Burón, I., Navas, P., German, J.B., Watkins, S.M. *et al.* (2010) Complex I-associated hydrogen peroxide production is decreased and electron transport chain enzyme activities are altered in n-3 enriched fat-1 mice. *PLoS ONE*, **5**, e12696.
30. Balaban, R.S., Nemoto, S. and Finkel, T. (2005) Mitochondria, oxidants, and aging. *Cell*, **120**, 483–495.
31. St-Pierre, J., Buckingham, J.A., Roebuck, S.J. and Brand, M.D. (2002) Topology of superoxide production from different sites in the mitochondrial electron transport chain. *J. Biol. Chem.*, **277**, 44784–44790.
32. Osaki, Y., Nishino, I., Murakami, N., Matsubayashi, K., Tsuda, K., Yokoyama, Y.I., Morita, M., Onishi, S., Goto, Y.I. and Nonaka, I. (1998) Mitochondrial abnormalities in selenium-deficient myopathy. *Muscle Nerve*, **21**, 637–639.
33. Hill, K.E., Motley, A.K., Li, X., May, J.M. and Burk, R.F. (2001) Combined selenium and vitamin E deficiency causes fatal myopathy in guinea pigs. *J. Nutr.*, **131**, 1798–1802.
34. Rederstorff, M., Krol, A. and Lescure, A. (2006) Understanding the importance of selenium and selenoproteins in muscle function. *Cell Mol. Life Sci.*, **63**, 52–59.
35. Martensson, J. and Meister, A. (1989) Mitochondrial damage in muscle occurs after marked depletion of glutathione and is prevented by giving glutathione monoester. *Proc. Natl Acad. Sci. USA*, **86**, 471–475.
36. Choksi, K.B., Boylston, W.H., Rabek, J.P., Widger, W.R. and Papaconstantinou, J. (2004) Oxidatively damaged proteins of heart mitochondrial electron transport complexes. *Biochim. Biophys. Acta*, **1688**, 95–101.
37. Kim, I., Rodriguez-Enriquez, S. and Lemasters, J. (2007) Selective degradation of mitochondria by mitophagy. *Arch. Biochem. Biophys.*, **462**, 245–253.
38. Tatsuta, T. and Langer, T. (2008) Quality control of mitochondria: protection against neurodegeneration and ageing. *EMBO J.*, **27**, 306–314.
39. Ding, W.X., Ni, H.M., Li, M., Liao, Y., Chen, X., Stolz, D.B., Dorn, G.W. 2nd. and Yin, X.M. (2010) Nix is critical to two distinct phases of mitophagy, reactive oxygen species-mediated autophagy induction and Parkin-ubiquitin-p62-mediated mitochondrial priming. *J. Biol. Chem.*, **285**, 27879–27890.
40. Moraes, C.T., Shanske, S., Tritschler, H.J., Aprille, J.R., Andreetta, F., Bonilla, E., Schon, E.A. and DiMauro, S. (1991) mtDNA depletion with variable tissue expression: a novel genetic abnormality in mitochondrial diseases. Am. J. Hum. Genet., **48**, 492–501.
41. Kim, I. and Lemasters, J.J. (2011) Mitochondrial degradation by autophagy (mitophagy) in GFP-LC3 transgenic hepatocytes during nutrient deprivation. *Am. J. Physiol. Cell Physiol.*, **300**, C308–C317.

Developmental Biology 361 (2012) 79–89

Contents lists available at SciVerse ScienceDirect

Developmental Biology

journal homepage: www.elsevier.com/developmentalbiology

Filamin C plays an essential role in the maintenance of the structural integrity of cardiac and skeletal muscles, revealed by the medaka mutant *zacro*

Misato Fujita [a,1,2], Hiroaki Mitsuhashi [b,1], Sumio Isogai [c], Takahiro Nakata [d], Atsushi Kawakami [a], Ikuya Nonaka [b], Satoru Noguchi [b], Yukiko K. Hayashi [b], Ichizo Nishino [b], Akira Kudo [a,*]

[a] Department of Biological Information, Tokyo Institute of Technology, 4259-B-33 Nagatsuta, Midori-ku, Yokohama 226-8501, Japan
[b] Department of Neuromuscular Research, National Institute of Neuroscience, National Center of Neurology and Psychiatry, 4-1-1 Ogawa-higashi, Kodaira, Tokyo 187-8502, Japan
[c] Department of Anatomy, School of Medicine, Iwate Medical University, 2-1-1 Nishitokuta, Yahaba, Shiwa 028-3694, Japan
[d] Department of Health Science, Ishikawa Prefectural Nursing University, 1-1 Gakuendai, Kahoku, Ishikawa 929-1210, Japan

ARTICLE INFO

Article history:
Received for publication 19 July 2011
Revised 5 October 2011
Accepted 6 October 2011
Available online 14 October 2011

Keywords:
Medaka mutant
Filamin C
Cardiac muscle
Skeletal muscle
zacro

ABSTRACT

Filamin C is an actin-crosslinking protein that is specifically expressed in cardiac and skeletal muscles. Although mutations in the filamin C gene cause human myopathy with cardiac involvement, the function of filamin C *in vivo* is not yet fully understood. Here we report a medaka mutant, *zacro* (*zac*), that displayed an enlarged heart, caused by rupture of the myocardiac wall, and progressive skeletal muscle degeneration in late embryonic stages. We identified *zac* to be a homozygous nonsense mutation in the *filamin C* (*flnc*) gene. The medaka filamin C protein was found to be localized at myotendinous junctions, sarcolemma, and Z-disks in skeletal muscle, and at intercalated disks in the heart. *zac* embryos showed prominent myofibrillar degeneration at myotendinous junctions, detachment of myofibrils from sarcolemma and intercalated disks, and focal Z-disk destruction. Importantly, the expression of γ-actin, which we observed to have a strong subcellular localization at myotendinous junctions, was specifically reduced in *zac* mutant myotomes. Inhibition of muscle contraction by anesthesia alleviated muscle degeneration in the *zac* mutant. These results suggest that filamin C plays an indispensable role in the maintenance of the structural integrity of cardiac and skeletal muscles for support against mechanical stress.

Introduction

Skeletal muscle and heart are the organs that produce physical force by muscle contraction, and muscle fibers are incessantly exposed to strong mechanical stress. To protect intracellular structures against such mechanical stress, muscle fibers express a variety of muscle-specific proteins that often form large complexes.

Two major protein complexes, the dystrophin-associated glycoprotein complex (DGC) and the integrin complex are known to have important roles in affording mechanical integrity to striated muscle. In skeletal muscle, these complexes, which are localized at the sarcolemma (Arahata et al., 1988; Mayer, 2003; Watkins et al., 1988) and myotendinous junctions (MTJs; (Bao et al., 1993; Samitt and Bonilla, 1990; Shimizu et al., 1989), where the muscle fibers are connected to tendon, link the subsarcolemmal actin cytoskeleton to the extracellular matrix (ECM) (Burkin and Kaufman, 1999; Campbell, 1995; Yoshida et al., 2000). Defects in the components of this DGC lead to muscular dystrophy (Bonnemann et al., 1995; Hoffman et al., 1987; Lim et al., 1995; Nigro et al., 1996; Noguchi et al., 1995; Roberds et al., 1994), an inherited muscular disorder characterized by progressive muscle degeneration, suggesting the importance of this linkage system for the integrity of muscle fibers. Muscle fibers specifically express α7β1 integrin, and a defect of α7 integrin causes muscular dystrophy, primarily affecting muscle fibers close to the MTJs (Hayashi et al., 1998; Mayer et al., 1997; Miosge et al., 1999), pointing to the importance of the integrin-based linkage for muscle integrity, particularly at MTJs. In heart, DGC and integrins are localized at the sarcolemma as well as at intercalated disks, which are the contact sites between cardiomyocytes (Anastasi et al., 2009; van der Flier et al., 1997).

The Z-disk is a huge multi-protein complex that constitutes the border of individual sarcomeres. This Z-disk plays a key role in the crosslinking of actin thin filaments of myofibrils to withstand the extreme mechanical force generated during muscle contraction. Z-disks are attached to the sarcolemmal DGC and integrin complexes at the sites of costameres via Z-disk-associated linker molecules (Ervasti, 2003). Recently, mutations in genes encoding Z-disk components have been found to be responsible for a group of muscle diseases termed myofibrillar myopathy, which is pathologically characterized by myofibrillar disorganization, including the degeneration of the

* Corresponding author. Fax: +81 45 924 5718.
E-mail address: akudo@bio.titech.ac.jp (A. Kudo).
[1] Misato Fujita and Hiroaki Mitsuhashi were equal contributors to this study.
[2] Present address. Section on Vertebrate Organogenesis, Program in Genomics of Differentiation, Eunice Kennedy Shriver National Institute of Child Health and Human Development, National Institutes of Health, MD 20892, USA.

0012-1606/$ – see front matter © 2011 Elsevier Inc. All rights reserved.
doi:10.1016/j.ydbio.2011.10.008

sarcomere structure (Selcen, 2008; Selcen et al., 2004). These reports suggest that Z-disk proteins have important roles in maintaining organized sarcomere structures.

Filamins are actin-crosslinking proteins first purified by their ability to bind and precipitate actin (Hartwig and Stossel, 1975; Stossel and Hartwig, 1975). Filamins are composed of 3 isoforms, filamins A, B, and C. All filamins consist of an N-terminal actin-binding domain followed by 24 immunoglobulin-like repeats, and they dimerize at the 24th repeat domain located at the C-terminus (Stossel et al., 2001). Filamins directly interact with more than 30 diverse proteins, and are involved in multiple cellular processes including cell–cell and cell–matrix adhesion, mechanoprotection, actin remodeling, and various intracellular signaling pathways (Feng and Walsh, 2004). Filamin C is a muscle-specific isoform and localizes at MTJs, costameres, Z-disks, and intercalated disks in mammal and avian muscles (Ohashi et al., 2005; van der Ven et al., 2000a). Interestingly, filamin C interacts with both DGC (Thompson et al., 2000) and integrin (Gontier et al., 2005; Loo et al., 1998), as well as with the Z-disk proteins myotilin (van der Ven et al., 2000b), FATZ-1 (Faulkner et al., 2000), and myopodin (Linnemann et al., 2010) through its C-terminal region. Such localization and protein interaction suggest that filamin C functions in maintaining the mechanical integrity of muscle cells. Recently, mutations in the filamin C gene were identified in patients having myofibrillar myopathy (Kley et al., 2007; Luan et al., 2010; Shatunov et al., 2009; Vorgerd et al., 2005). These patients frequently develop cardiac abnormalities in addition to skeletal myopathy, suggesting the essential role of filamin C in both skeletal and cardiac muscles. To investigate the function of filamin C *in vivo*, Dalkilic et al. (2006) generated *filamin C*-deficient mice having a deletion of the last 8 exons of *Flnc*. This deficient mouse shows fewer muscle fibers or primary myotubes than normal and abnormal rounded fibers, suggesting defects in primary myogenesis; however, this mouse does not present any cardiac defects, which indicates a partial-loss-of-function. Since these mice die *in utero* or live only a short while after birth, further detailed observations cannot be carried out.

Recently, zebrafish have emerged as an alternative model organism to study the vertebrate muscular system and to isolate new dystrophy-causing genes/pathways (Guyon et al., 2007; Steffen et al., 2007). A deficiency of DGC or integrin-linked kinase causes a muscular dystrophic phenotype in zebrafish embryos (Bassett et al., 2003; Cheng et al., 2006; Gupta et al., 2011; Guyon et al., 2005; Postel et al., 2008), suggesting that their functions are likely to be analogous to those in humans. In zebrafish embryos, the DGC is localized initially at the junctional area, where the ends of muscle fibers attach to the myosepta, corresponding to the myotendinous junction (MTJ). Loss of DGC causes muscle fiber detachment at MTJs, indicating compromised adhesion between muscle fibers and the ECM of myosepta. Medaka (*Oryzias latipes*), another teleost fish, has the experimental advantages of external development, transparency, and quick production of a number of embryos, similar to the zebrafish. Unlike zebrafish, however, various medaka inbred strains have been established; and the medaka genome, which is about one-half of the size of the zebrafish genome, is almost fully sequenced and aligned, indicating that the medaka has powerful advantages for the application of forward genetics (Ishikawa, 2000; Wittbrodt et al., 2002).

Here, we identified a medaka mutant, *zacro* (*zac*), that has a nonsense mutation, resulting in an early truncation at the 15th immunoglobulin-like repeat of the medaka orthologue of filamin C. This mutation causes myocardiac rupture in the ventricle. Although this mutant displayed normal myogenesis in myotome muscles during early stages of embryonic development, its myofibrils gradually degenerated and became disorganized in later stages. Detailed histological analysis suggests an indispensable role of filamin C in the maintenance of the muscle structure rather than in its formation in both heart and skeletal muscles.

Materials and methods

Medaka strains and mutant screening

All studies requiring wild-type medaka (*O. latipes*) were carried out by using the Qurt strain, which was derived from the southern population (Wada et al., 1998). Fish were maintained in an aquarium system with re-circulating water at 28.5 °C. Embryos were obtained from natural spawning, and incubated at 28 ± 2 °C. Stages were determined as previously described (Iwamatsu, 2004). *N*-ethyl-*N*-nitrosourea (ENU) was used for mutagenesis, and a standard genetic F3 screening for mutations affecting embryogenesis were performed as described earlier (Ishikawa, 1996; Ishikawa et al., 1999). The *zac* mutant was identified by microscopic inspection as a Mendelian-inherited recessive lethal mutation that caused a phenotype characterized by congestion in the blood vessels and pericardial edema.

Positional cloning

zac heterozygous fish, which were maintained on the southern Qurt genomic background, were mated with the northern HNI strain fish (Hyodo-Taguchi, 1980) to generate F1 families. Embryos for the genetic mapping were obtained from inter-crosses of F1 *zac* carriers. To locate the genetic linkage, we conducted bulk segregant analysis on pools of genomic DNA from *zac* mutants and wild-type embryos by using sequence tagged site (STS) markers on the medaka genome (Kimura et al., 2004). The *zac* region was narrowed down by using additional STS markers, AU171271 and Olb2110h (Naruse et al., 2000), and newly designed restriction fragment length polymorphism (RFLP) markers, HAL and KCND2 (HAL; 5′-GGATGGGCAGATGCCAAATATG-3′ and 5′-GTCCCGTTGATCAGAGCCAG-3′/MboI, KCND2; 5′-CAGCAGGTGTAGCGGCATG-3′ and 5′-GTTGGCCATCACTGATATGGC-3′/AfaI). cDNAs of *flnc* from *zac* mutant and wild-type embryos were amplified, and verified by sequencing. The full-length cDNA of *flnc* was cloned by PCR using primers including XbaI restriction enzyme sites [5′-CAATCTAGACAAGGAACAAGCC-3′ and 5′-GAATCTAGACCACCATTTAGCC-3′], and was sequenced. We obtained 2 different *flnc* clones, which appeared to be splice variants. To confirm the linkage between the *zac* mutation and *flnc* gene, we performed allele-specific PCR using 2 independent outer primers [5′-TTCAGTTGGAGGACATGGGAT-3′ and 5′-GACACCTGCAACACAACTCTA-3′] in combination with either a wild type-specific antisense primer [5′-CTTGCAGGTCACCTTTCCTTT-3′] or a mutant-specific one [5′-CTTGCAGGTCACCTTTCCTTA-3′]. We also performed 5′-RACE and 3′-RACE to obtain full-length sequence information on *flnc* cDNA. The sequences of the medaka *flnc* have been deposited in GenBank under the accession numbers AB639344 and AB639345.

Birefringence assay

Embryos were dechorionated at stage 27. Muscle birefringence was analyzed at stages 32 and 34 by placing anesthetized embryos on a glass dish and observing them with an underlit dissecting scope (Olympus, SZX12) having 2 polarizing filters (Olympus, SZX-P0 and SZX2-AN). The top polarizing filter was twisted until only the light refracting through the striated muscle was visible.

Histological analysis

Embryos were fixed overnight at 4 °C in 4% paraformaldehyde (PFA) in phosphate-buffered saline pH 7.4 (PBS), dehydrated by ethanol, and embedded in a resin (Technovit 8100, Kulzer Heraeus) according to the manufacturer's instructions. Sections were cut at 2 μm and stained with Harris's hematoxylin and Eosin Y or Masson trichrome staining buffer (SIGMA).

Whole-mount RNA in situ hybridization

Whole-mount RNA *in situ* hybridization was performed as previously described (Inohaya et al., 1995; Inohaya et al., 1999). Digoxigenin-labeled antisense RNA probes for cardiac myosin light chain 2 (*cmlc2*), desmin (*des*), *flnc*, *myf5*, *nkx2.5*, *tbx5a*, and ventricular myosin heavy chain (*vmhc*) were used. The primer sets used for cloning the respective probes are listed below.

cmlc2 F: AATGTCTTTTCCATGTTYGARC
R: CAGATTCAGCAGTTTAARGARG and CTCCTCTTTCTCATCHCCATG
des F: AACAACCAGCCAACCATGAGC
R: ACAGATGTAGTTATCCTGCAGG
flnc F: GCTCCAGAGGAAATTGTGGAC
R: CTCACACCTTTAGGCTGTAGC
myf5 F: ATCCACTTCTTCTCCCCAGC
R: TTTCTCCTCAGAGAGAACCG
*nkx2.5*F: TTCTCTCAGGCGCAGGTGTACGAGC
R: GCDGGGTAGGYGTTGTA
tbx5a F: GTCTGAGATTTTCCGAGCTCC
R: CTCTCTCTAGACTCGAGTTGGTCCTTCTTGTGTTCTCCC
vmhc F: GGAGCTGGATGATGTGGTTTC
R: CATGGGCTAAGGCGTTCTTGGC
(R: A,G. Y: C,T. H: A,C,T)

Injection of morpholino antisense oligonucleotide (MO)

We obtained a specific MO (Gene Tools) to interfere with *flnc* translation. The MO [5′-GGCCATCATGTTGGCTTGTTCCTTG-3′] was dissolved at concentrations from 100 to 1000 μM in nuclease-free water. Approximately 0.5 nl of MO solution or standard control MO [5′-CCTCTTACCTCAGTTACAATTTATA-3′] was injected into 1-cell-stage embryos.

Whole-mount immunofluorescence

Dechorionated embryos were anesthetized in 0.02% tricaine methanesulfonate and fixed in 4% PFA in PBS at 4 °C overnight. We used chilled methanol at −20 °C as the fixative for anti-laminin antibody, and IHC Zinc fixative (BD Biosciences) for anti-γ-actin antibody. After fixation, embryos were dehydrated in a graded series of methanols (25–50–75%) and stored in 100% methanol at −20 °C. Embryos were rehydrated in a graded series of methanols (75–50–25%) and washed 3 times for 15 min each time in MABTr (0.1 M maleic acid and 150 mM NaCl containing 0.1% Triton X-100) and subsequently in MABDTr (MABTr with 1% BSA and 1% DMSO) twice for 30 min each time. Following blocking with 5% goat serum in MABDTr for 30 min, the embryos were incubated with primary antibodies at 4 °C overnight. The following antibodies were used: anti-filamin C (SIGMA HPA006135; 1:100), anti-vinculin (SIGMA V4505; 1:50), anti-α-actinin (SIGMA A7811; 1:500), anti-integrin β1D (Millipore MAB1900; 1:25), anti-β-sarcoglycan (Novocastra NCL-b-SARC; 1:50), anti-slow muscle myosin heavy chain (F59, DSHB; 1:100), anti-FAK pY397 (Invitrogen 44-625G; 1:100), anti-dystrophin (SIGMA D8043; 1:100), anti-β-dystroglycan (Novocastra NCL-b-DG; 1:100), and anti-phospho-paxillin (Cell Signaling Technology #2541; 1:50). Rabbit polyclonal anti-cytoplasmic γ-actin antibody was previously characterized (Nakata et al., 2001), and used at a dilution of 1:100. Embryos were washed 6 times in MABDTr for 15 min each time, and then incubated with Alexa488-conjugated anti-rabbit IgG or Alexa568-conjugated anti-mouse IgG (Molecular Probe; 1:800) at 4 °C overnight. Primary and secondary antibodies were diluted in Can Get Signal immunostain solution A (TOYOBO). After 6 more washings in MABTr, the embryos were whole-mounted on glass slides and observed with a confocal microscope (LSM 700, Zeiss).

Electron microscopy

For observation using transmission electron microscope (TEM), embryos were dechorionated and fixed at stage 27, 29, 30, 32 or 36 in 100 mM cacodylate buffer (pH 7.4) containing 2% glutaraldehyde and 4% PFA at 4 °C overnight. Samples were post-fixed in 0.06 M s-collidine buffer (pH 7.2) containing 1.3% osmium tetroxide and 0.5% lanthanum nitrate, dehydrated by passage through a graded series of ethanols, and finally embedded in Epon 812 (Taab). Longitudinal sections (120 nm) were stained with 3% uranyl acetate for 20 min and then with 0.4% lead citrate for 5 min. Sections were viewed with a Tecnai Spirit transmission electron microscope (FEI) or a Hitachi H-7100 or H-7650 electron microscope (Hitachi).

For observation using scanning electron microscopy (SEM), embryos were fixed in 0.1 M phosphate buffer (PB, pH 7.4) containing 2.5% glutaraldehyde and 2% PFA. The yolk were removed from the embryo with forceps to expose the heart, and postfixed for 2 h in 1% osmium tetroxide in PB at 4 °C. The embryos were then rinsed in PB, dehydrated in a graded series of ethanol, frozen in t-butyl alcohol, then freeze-dried *in vacuo* with an Eiko ID-2. The embryos were mounted on a metal stub, osmium-coated by using a Filgen OPC60A, and observed with an HS-6 electron microscope (Hitachi).

Muscle relaxation assay

Embryos were incubated with anesthetized in 0.0015% tricaine methanesulfonate in embryo medium for 48 h from stages 27 to 32 to prevent muscle contractions. Treated and untreated embryos were immunostained with F59 antibody obtained from the Developmental Studies Hybridoma Bank at stage 32, and the number of somites with muscle-fiber degeneration was counted.

Results

Enlarged ventricle and muscle disorganization in zac mutants

zacro (*zac*) is a recessive, embryonic-lethal mutant obtained by ENU (*N*-ethyl-*N*-nitrosourea) mutagenesis. *zac* mutants were characterized by an abnormally enlarged heart with a gradually reduced blood flow. The normal medaka heart starts to beat at stage 24, and blood flow begins at stage 25. No difference was observed until stage 25 in *zac* embryos; however, by stage 28 prior to the heart looping, *zac* mutants showed blood congestion in the ventricle along with pericardial edema (Figs. 1A, B). Ruptures in the myocardium layer were detected in the *zac* mutants at stage 27, especially in the dorsal-right myocardium of the ventricle (Figs. 1C, D asterisk). As the endocardium was intact in *zac* mutants, we speculate that the blood accumulation was caused by ineffective contraction of the torn myocardium. *zac* mutants appeared to be normal in their somite differentiation during the early stages of somitogenesis; however, by stage 32, they frequently exhibited an abnormal curvature with their tails dorsally up instead of having the normal flat body axis (Figs. 1E, F). We further analyzed the birefringence of myotome muscle of *zac* mutants by using polarized filter microscopy. Birefringency is used to assess muscle organization in zebrafish models of muscle disease (Granato et al., 1996). Wild-type embryos from stage 32 onwards displayed high birefringence due to the ordered array of their myofilaments (Figs. 1G, I), whereas *zac* mutants displayed patchy birefringence at this stage (Fig. 1H), indicating muscle disorganization in some somites. Muscle disorganization in the *zac* mutant continued to progress, and most of the somites lost their birefringence by stage 34 (Fig. 1J). Histological analysis revealed that orientation of each myotube was severely disorganized by stage 40 (Figs. 1K, L).

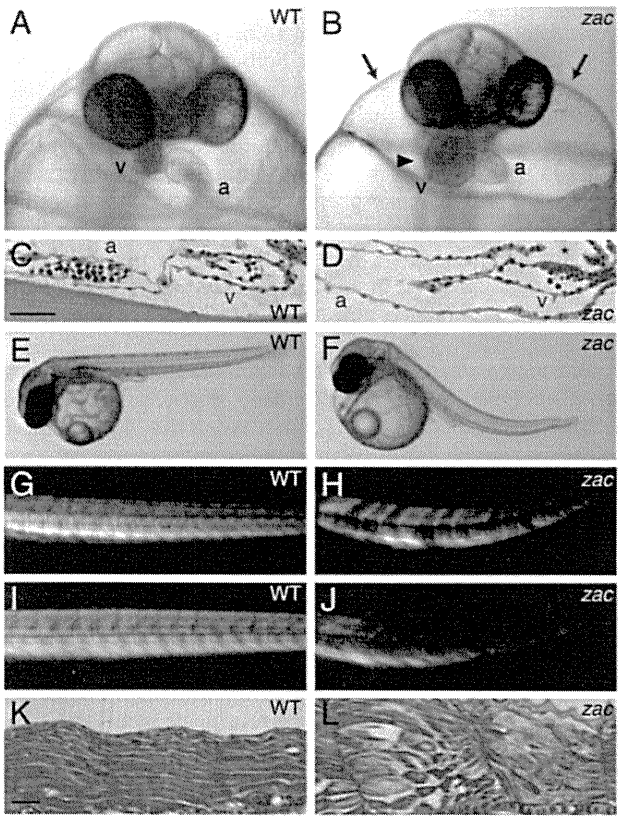

Fig. 1. Cardiac and skeletal muscle phenotypes of *zac* mutants. Embryos from the wild-type (A, C, E, G, I, K) and *zac* mutants (B, D, F, H, J, L). (A, B) Ventricular enlargement in *zac* mutants. Frontal views at stage 28. Dorsal is to the top. Blood cell accumulation in the ventricle (B, arrowhead) and cardiac edema (B, arrows) are visible. a; atrium, v; ventricle (C, D) Hematoxylin and eosin staining of a sagittal section of heart at stage 27. Rostral is to the left. Only the myocardial wall has a rupture (D, asterisk). Scale bar: 20 μm in "C." (E, F) Whole view from the lateral side at stage 32. *zac* mutants show body curvature. (G–J) Birefringence of skeletal muscle at stage 32 (G, H) and stage 34 (I, J). Rostral is to the left. *zac* mutant shows patchy birefringence at stage 32 and overall reduction in birefringence at stage 34. (K, L) Masson trichrome staining of horizontal sections at stage 32. Rostral is to the right. Striated patterns of sarcomeres can be seen in many muscle cells, but some myofibers have severely degenerated in the *zac* mutants. Scale bar in "K": 20 μm.

After hatching, *zac* mutants were not able to swim normally, and they died around 14 days post-fertilization. These phenotypes indicate that the *zac* mutation affected both cardiac and skeletal muscles.

Nonsense mutation in flnc in zac mutants

We performed positional cloning to identify the responsible gene in *zac* mutants. By using sequence-tagged site (STS) markers (Kimura et al., 2004), we mapped the *zac* gene to the marker MF01SSA047D04 on the medaka linkage group 6 (Fig. 2A). We searched the expressed sequence tag (EST) markers around the MF01SSA047D04, and found zero and 2 independent recombinants by using AU171271 and Olb2110h, respectively. Therefore, the *zac* gene was placed in the vicinity of AU171271 between MF01SSA047D04 and Olb2110h (Fig. 2A). We further performed fine mapping by utilizing an additional marker, histidine ammonia-lyase (*HAL*), which gave 1 recombinant and narrowed down the *zac* locus. We also found zero recombinants by using another marker, the potassium voltage-gated channel, Shal-related subfamily, member 2 (*KCND2*). Though the genomic sequence encompassing the *zac* locus contained several open reading frames (ORFs), one of them encoded a protein highly homologous to human filamin C, a cardiac and skeletal muscle-specific isoform of the filamin family.

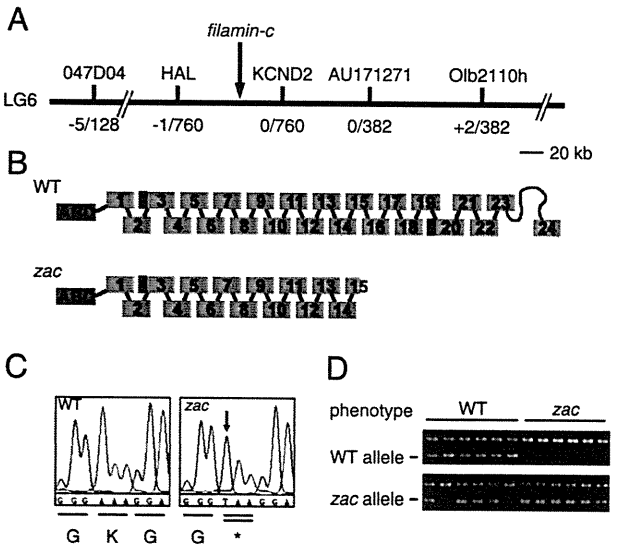

Fig. 2. Positional cloning of *zac* gene (A) Map of the genomic region containing the *zac* gene. The *zac* locus is mapped on the medaka linkage group (LG) 6 by using M-markers, and *flnc* is located in the candidate region. HAL, histidine ammonia-lyase and KCND2, potassium voltage-gated channel, Shal-related subfamily, member 2. Recombination frequencies for the respective markers are shown below. (B) Schematic drawings of filamin C protein in wild-type and *zac* mutant. The actin-binding domain (ABD) is located at N-terminal followed by 24 repeats of filamin domains. The red region between the 2nd and 3rd repeats indicates the unique splicing variation in medaka fish. The green box between the repeats 19th and 20th is a unique sequence in filamin C members. There is only one hinge sequence between the repeat 23rd and 24th in the medaka filamin C. (C) Chromatogram of the cDNA sequence containing a nonsense mutation from A to T in a coding region of *flnc* (arrow). (D) Linkage of *zac* mutation with *flnc* as shown by allele-specific genotyping PCR. WT indicates phenotypically wild-type embryos, so some are genotypically heterozygotes revealing both WT and zac alleles' PCR products and others are genotypically wild-type having WT allele's PCR product only. All *zac* mutants are genotypically homozygotes, which show the zac allele's PCR products only.

The sequence analysis revealed that the medaka *flnc* had a high degree of homology (approximately 77% amino acid identity) to the human *FLNC* (Supplementary Fig. 1). The overall structure of medaka filamin C consisted of the actin-binding domain (ABD) and 24 immunoglobulin-like repeats with a hinge region between the 23rd and the 24th repeats (Fig. 2B). Although there was no spacer region between the 15th and the 16th repeats, as found in chicken *Flnc/cgABP260* (Ohashi et al., 2005) and in some human *FLNCs* (Supplementary Fig. 1), the medaka *flnc* had a C-isotype-specific insertion sequence between the 19th and the 20th repeats (green box in Fig. 2B; blue underline in Supplementary Fig. 1), which is also seen in mouse *Flnc* (Dalkilic et al., 2006). We also found a novel splicing variation of an additional 39 amino acids between the 2nd and 3rd repeats (red box in Fig. 2B).

We sequenced the entire coding sequence of medaka *flnc* from the *zac* mutant and the wild-type sibling alleles and found that the *zac* mutant had a nucleotide substitution from A to T at the first base of codon 1680 (Fig. 2C; AAA to TAA). As a result, this mutation changed the lysine residue to a stop codon (K1680X), causing premature termination in the 15th immunoglobulin-like repeat. This mutation was detected with 100% identity by PCR using allele-specific primers (Fig. 2D).

In the medaka genome database from Ensembl, there is one more filamin C ortholog, which is notated as FLNC (2 of 2). This predicted gene is located mostly in the ultracontig278 and partially in the scaffold698_contig104802. To find the possibility of functional contribution, we examined the sequence similarity of this gene compared to the human filamin C and the medaka filamin C investigated in this study (Supplementary Fig. 2). FLNC (2 of 2) is described as "ol filamin c #3" in this figure. The FLNC (2 of 2) contains 16 filamin-repeats from 9th to 24th repeat of the regular filamin C, and has one hinge region between 23rd and 24th repeat. About three fourth of filamin C-specific region (UR) is pulled out and N-terminal domains of the

actin binding domain and 1–8th repeats are missing. Although the entire sequence is well conserved and the feature of having single hinge represents filamin C, the lack of N-terminal domains is critical. This gene might be termed as "ol flnc 9–24" (Stossel et al., 2001) and functional redundancy would not be expected as for filamin C.

mRNA expression of flnc is markedly reduced in zac mutants

The pattern of *flnc* expression was analyzed by whole-mount RNA *in situ* hybridization. *flnc* expression was first evident in somites and at the rostral tip of notochord at the onset of somitogenesis. Subsequently, by the 6-somite stage, the expression of *flnc* was detected in the cardiac precursor cells in the anterior lateral-plate mesoderm (Fig. 3A). After migration of the myocardial precursor cells towards the midline, the expression of *flnc* was detected in both the atrium and ventricle (Fig. 3C). These expressions of *flnc* in the somites, the rostral tip of the notochord, and the cardiac muscles continued in subsequent stages (Fig. 3E). At later stages, additional expression was seen in the muscles of the pectoral fin joint and head (data not shown). Although the pattern of expression of *flnc* did not differ between the wild-type and *zac* mutants, the level of expression was reduced in the latter (Figs. 3B, D, F).

To further identify whether this lower expression of *flnc* in *zac* mutants was caused by the transcriptional down-regulation or not, we generated a transgenic medaka line expressing EGFP under the regulation of a 3 kb-*flnc* promoter. Both in the wild-type and *zac* mutants, the EGFP transgene was expressed at a similar level (Figs. 3G, H), demonstrating that the transcription of the *flnc* gene was not affected by the *zac* mutation. Moreover, the reduced mRNA expression of *flnc* in *zac* mutants was detected before the appearance of abnormal cardiac and muscular phenotypes (Figs. 3A, B), suggesting that the reduction was not caused by any morphological effect in the *zac* mutants. Taken together, these results suggest that the apparently lower expression of *flnc* in *zac* mutants may have been due to the instability of the mutated mRNAs, as often observed in other cases (Baker and Parker, 2004).

To confirm whether the defect in *flnc* was sufficient to cause the *zac* phenotype, we used morpholino antisense oligonucleotides (MO) targeting the translation of *flnc*. When the MO was injected at a dose of 400 μM, 13% of the injected embryos displayed a *zac*-like cardiac phenotype including the myocardial ruptures ($n=94$; Figs. 3I, J). In contrast to the heart phenotype, we did not observe an abnormal phenotype in the skeletal muscles of the MO-injected embryos. It appears that the MO may have required a longer time before producing the skeletal muscle phenotype, but the effect of MO might not have been strong enough to affect the skeletal muscles. We tested higher concentrations of MO (500–1000 μM); however, the overall shape of the injected embryos was severely deformed.

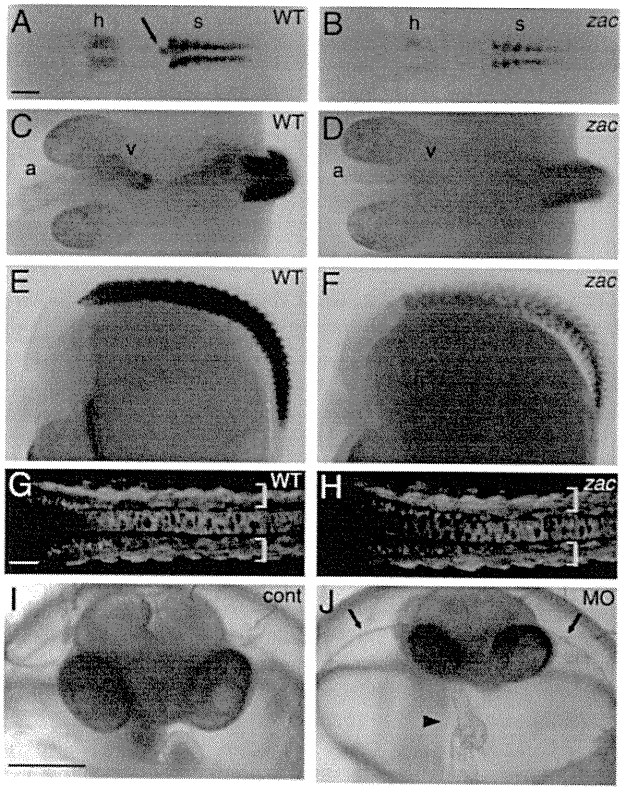

Fig. 3. Expressions of medaka *flnc* in notochord and cardiac and skeletal muscles. Wild-type (A, C, E, G) and *zac* mutant embryos (B, D, F, H). (A–F) Whole-mount RNA *in situ* hybridization analysis of *flnc* expression at stage 22 (A, B) and stage 27 (C–F). Dorsal views (A–D) and lateral views (E, F). Rostral is to the left. *flnc* expression is seen in bilateral cardiac precursor cells (h), somites (s), and the anterior tip of the notochord (arrow). Both atrium (a) and ventricle (v) express *flnc*. Note that *flnc* mRNA expression is reduced in *zac* embryos (B, D, F). (G, H) *flnc* expression visualized in the *flnc* promoter transgenic medaka at stage 26. Dorsal views of the trunk. Rostral is to the left. The level of EGFP expression is not decreased in *zac* mutants, demonstrating that the decrease in the *flnc* mRNAs may be due to instability of mutated *flnc* mRNAs. Yellow and red brackets indicate somites and notochord, respectively. (I, J) Phenocopy by injection of MO. Stage 28, Head frontal views. Dorsal is to the top. Embryos injected with the control MO show the normal appearance (I). However, embryos injected with *flnc*-MO show the cardiac rupture in the ventricle (J: arrowhead) and edema (J: arrows). Scale bars: 100 μm in "A", 50 μm in "G" and 200 μm in "I".

zac mutation affects the maintenance of the muscle structure rather than its formation

Since the expression of *flnc* in medaka embryos was detected in the early stage of development (see Fig. 3), we investigated whether the *zac* mutation affected the differentiation of cardiac or skeletal muscle cells by examining the expression of various differentiation marker genes. The expression patterns and levels of cardiac differentiation markers, such as *nkx 2.5*, *tbx5a*, *des*, *cmlc2*, and *vmhc*, were not changed in *zac* hearts at stage 27 (Figs. 4A, B: *cmlc2*, C, D: *des*, the data for *nkx 2.5*, *tbx5a*, and *vmhc* are not shown). The expressions of muscle differentiation markers such as *myoD*, *myf5*, and *des* were also normal in the trunk and tail up to stage 30 (Figs. 4E–H). These results suggest that the early differentiation of cardiac and skeletal muscle cells was not affected in the *zac* mutants.

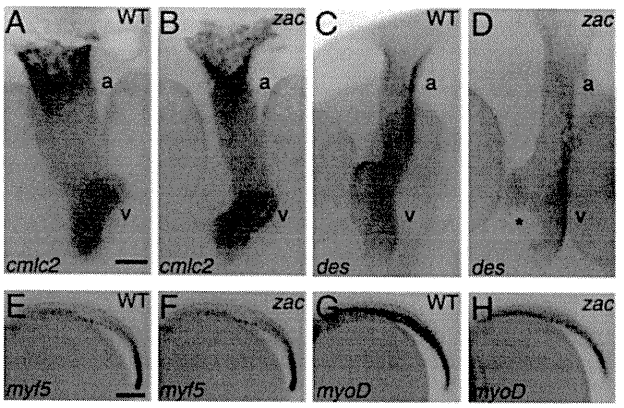

Fig. 4. Expressions of differentiation marker genes in cardiac and skeletal muscle development (A–D). Whole-mount RNA *in situ* hybridization for the expression of cardiomyocyte markers, *i.e.*, *cmlc2* (A, B) and *des* (C, D) at stage 27. Wild-type (A, C) and *zac* mutants (B, D). Dorsal view (A, B) and ventral view (C, D) are shown. Rostral is to the top. Differentiation of cardiomyocytes looks normal. A rupture of the myocardium in the *zac* ventricle is indicated by the asterisk. a; atrium and v; ventricle (E–H) Whole-mount RNA *in situ* hybridization for the expression of muscle markers *myf5* (E, F) and *myoD* (G, H) at stage 27. Wild-type (E, G) and *zac* mutants (F, H). Lateral views. Head is to the left. Both genes show normal expression patterns in the *zac* mutant. Scale bars: 20 μm in "A" and 200 μm in "E".